



Federal Office of Meteorology  
and Climatology MeteoSwiss

MASTER THESIS

---

**Radial wind velocity retrieval  
from Doppler radar and lidar measurements  
using Deep Learning**

---

ECOLE POLYTECHNIQUE FÉDÉRALE DE LAUSANNE  
ENVIRONMENTAL SCIENCES AND ENGINEERING  
LTE, REMOTE SENSING LABORATORY

*Author*

Maëlle ROMERO GRASS

*Supervisors*

Alexis BERNE, EPFL  
Maxime HERVO, Meteoswiss

September 24, 2020



# Abstract

A Pulse-Doppler Radar Wind Profiler (RWP) is an active remote sensing instrument used in meteorology whose output product is a 3D wind field. A new method to retrieve radial wind velocity from spectrograms using Convolutional Neural Networks is introduced. The collection of data is provided by the Federal Office of Meteorology and Climatology MeteoSwiss and collected in Payerne, Switzerland. It covers the summer months of the year 2020.

As a first step, spectrograms are split into different classes as follows: (0) no visible/measured wind, (1) visible wind only, (2) massive bird contamination (3) slight contamination and wind still visible. In terms of accuracy, precision and recall, the model achieves a solid performance of 94% on the test set with a tendency to mix classes 1 and 2 with class 3.

Spectrograms either too heavily contaminated (class 2) or lacking a wind signal (class 0) are discarded in a second phase. A Doppler lidar provides the radial velocity shift for each spectrogram. Across the test set, a  $R^2$  of 0.97 is obtained along with a mean absolute error of  $0.22 \text{ m s}^{-1}$ .

The study undoubtedly opens up a new range of possibilities regarding the processing of wind profiler measurements. Modern techniques have been successfully deployed, and coupling them with the existing and approved algorithms might strengthen the output product robustness.

Keywords: Pulse-Doppler Radar Wind Profiler (RWP), Convolutional Neural Network (CNN), Machine Learning (ML), Doppler lidar, wind velocity retrieval, intermittent bird clutter

Un radar Doppler profileur de vent est un instrument de télédétection actif utilisé en météorologie dont le produit final est un champ de vent. Une nouvelle méthode permettant d'extraire la vitesse de vent radiale à partir des spectrogrammes à l'aide de réseaux de neurones convolutifs (en anglais CNN, Convolutional Neural Network) est présentée. Le jeu de données est offert par l'Office fédéral de météorologie et de climatologie MétéoSuisse et collecté à Payerne, en Suisse. Il couvre les mois d'été de l'année 2020.

Dans un premier temps, les spectrogrammes sont divisés en différentes classes comme suit : (0) pas de vent visible/mesuré, (1) vent visible seulement, (2) contamination massive par les oiseaux et (3) contamination légère et vent encore visible. En termes d'exactitude, de précision et de rappel, le modèle atteint une performance satisfaisante de 94 % sur le test, avec une tendance à confondre les classes 1 et 2 avec la classe 3.

Les spectrogrammes trop contaminés (classe 2) ou ne présentant pas de vent visible (classe 0) sont mis à l'écart dans un deuxième temps. Un lidar Doppler fournit la vitesse radiale pour chaque spectrogramme. Un  $R^2$  de 0.97 et une erreur absolue moyenne de  $0.22 \text{ m s}^{-1}$  sont obtenus sur le jeu de données test.

L'étude ouvre un nouvel éventail de possibilités concernant le traitement des mesures issues de radars profileurs de vent. Les techniques déployées l'ont été avec succès, et en conjugaison avec les algorithmes existants et approuvés elles pourraient renforcer la robustesse du produit final.

Mots-clefs : radar Doppler profileur de vent, réseau neural convolutif (CNN), Machine Learning (ML), lidar Doppler, extraction de la vitesse de vent radiale, contamination par les oiseaux

# Acknowledgements

I gratefully thank Meteoswiss, especially Maxime Hervo and Alexander Haefele for offering the project, the collection of the data and the supervision as well as Loris Foresti for contributing with his external expertise.

A special and warm thanks is extended to Benoît Crouzy and Gian-Duri Lieberherr for their help, availability and genuine goodwill along with the MDSB team for the infrastructure made available that offered sufficient computational power to make this thesis possible.

Last but not least, I also deeply appreciated the efficient support of Prof. Alexis Berne, including his valuable feedback.

# Contents

<b>Abstract</b>	<b>I</b>
<b>Acknowledgements</b>	<b>III</b>
<b>Symbols</b>	<b>VI</b>
<b>Introduction</b>	<b>1</b>
<b>1 Radar Wind Profiler</b>	<b>2</b>
1.1 PCL 1300 . . . . .	2
1.1.1 Operational informations . . . . .	2
1.1.2 Measurement principle . . . . .	3
1.1.3 Vertical motion . . . . .	4
1.2 Current signal processing . . . . .	4
1.2.1 Merritt's algorithm . . . . .	5
1.2.2 Statistical peak identification . . . . .	5
1.2.3 Multipeak and consensus algorithms, quality controls . . . . .	7
1.2.4 Wind vector calculation . . . . .	7
1.3 Bird contamination . . . . .	8
1.3.1 Classification of contaminated spectrum with Neural Networks .	9
1.3.2 Gabor filtering algorithm . . . . .	9
<b>2 Dataset</b>	<b>11</b>
2.1 Description . . . . .	11
2.1.1 Data sources . . . . .	11
2.1.2 Visualisation . . . . .	12
2.1.3 Disk space considerations . . . . .	15
2.2 Doppler wind lidar . . . . .	15
2.2.1 Operational informations . . . . .	15
2.2.2 Measurements pairing . . . . .	16
2.2.3 Resolution volumes . . . . .	17
2.3 Coherency evaluation . . . . .	17
2.3.1 Precipitation and bird contamination . . . . .	19
2.3.2 Temporal and spatial resolutions . . . . .	21
<b>3 Models and methods</b>	<b>24</b>
3.1 Classification . . . . .	24
3.1.1 Manual classification tool . . . . .	24
3.1.2 Spectrogram and additional features preprocessing . . . . .	26

3.1.3	Classification model . . . . .	27
3.1.4	Loss and metrics . . . . .	29
3.2	Regression . . . . .	29
3.2.1	Manual selection of coherent dataset . . . . .	29
3.2.2	Spectrogram and additional features preprocessing . . . . .	30
3.2.3	Regression model . . . . .	31
3.2.4	Loss and metrics . . . . .	32
<b>4</b>	<b>Results and discussion</b>	<b>33</b>
4.1	Classification . . . . .	33
4.2	Regression . . . . .	37
4.3	Discussion . . . . .	40
4.3.1	Model generalisation . . . . .	40
4.3.2	Dataset size . . . . .	40
4.3.3	Input data . . . . .	41
4.3.4	Real time implementation . . . . .	41
<b>Conclusion</b>		<b>43</b>
<b>Appendix A</b>		<b>44</b>
<b>Appendix B</b>		<b>56</b>
<b>Bibliography</b>		<b>58</b>

# Symbols

$\lambda$	wavelength	m
$f$	operational frequency	Hz
$c$	speed of light	$\text{m s}^{-1}$
$f_r$	radial Doppler frequency shift	Hz
$V_r$	radial Doppler velocity shift	$\text{m s}^{-1}$
$u_x, u_y, u_z$	wind velocity vectors	$\text{m s}^{-1}$
$V_{rx}, V_{ry}$	Doppler velocity shifts of two opposite oblique beams	$\text{m s}^{-1}$
$V_{rz}$	Doppler velocity shifts of the vertical beam	$\text{m s}^{-1}$
$\theta_x, \theta_y$	elevation angles from vertical ( $0^\circ$ is vertical)	rad
$\phi_x, \phi_y$	azimuth angles ( $0^\circ$ is North)	rad

## Subscripts

$r$	radial, i.e. in the direction of the beam
$x, y$	identifying two opposite oblique beams (northeast/southwest or northwest/southeast)
$z$	identifying the vertical beam

## Comment on indices

Matlab indices start with 1 and Python with 0. Beam numbers are given starting from 1 and gate numbers from 0. Both remain coherent in the codes.

# Introduction

MeteoSwiss operates radar wind profilers located in Schaffhausen, Grenchen and Payerne. They form part of an extensive monitoring network supplemented by the so-called COSMO model for numerical weather forecast ([Windprofiler - MeteoSwiss 2020](#)). In particular, the association of precise measurements and high-resolution forecasts provides an estimation of the wind field and weather development around Switzerland's nuclear power plants. In case of accident, it would allow an estimation of the plume displacement ([Meteorology for nuclear accidents - MeteoSwiss 2020](#)).

Wind profiler measurements post-processing can be impacted by non atmospheric targets, predominantly migrating birds. The induced clutter results in missing data. The issue is well-known for more than 25 years. The objective has became the identification and removal of contaminated spectra. It was first achieved by [Merritt \(1995\)](#) thanks to statistical tests. Indeed, atmospheric signals and point targets show exponential and non-exponential power distributions respectively. Later, [Kretzschmar et al. \(2003\)](#) and [H. Weber \(2005\)](#) tested Neural Networks fed with features stemming from the power distribution. Most recently, [Lehmann \(2012\)](#) proposed a Gabor transform and subsequent filter, focusing on getting rid of the contamination before computing the spectrograms.

The present work fits into a larger framework, with the intention of evaluating the performance of Convolutional Neural Networks on both bird clutter identification and radial wind velocity retrieval. The input data is wind profiler spectrograms computed with a discrete Gabor transform. A Doppler lidar located a few meters away is used to determine the radial Doppler velocity shift of each spectrogram.

After a chapter dedicated to the wind profiler, the dataset is described and visually presented into details for the sake of clarity. The models and methods are introduced and the results obtained unveiled. A last section is devoted to suggestions for future research. All codes are available at <https://github.com/MaL-R/RWP>.

# 1 Radar Wind Profiler

Remote sensing, allowing measurements to be taken without physical contact with the target, has proven effective in many environmental applications, including meteorology. A wind profiler is a radar whose output product is a 3D wind field. The name "profiler" results from the capability of the instrument to take measurements at equidistant heights called *gates* and thus to produce a wind profile.

Please note that the theoretical background of this section is intended to provide a brief overview of the physical principles and wind profiler operational aspects necessary to conceive the motivations and development of this work. For an in-depth insight, one might refer to [Fukao et al. \(2014\)](#).

## 1.1 PCL 1300

### 1.1.1 Operational informations

The present thesis is based on data acquired by the PCL1300 wind profiler located in Payerne in 2020. It is supplied by the company Degreane along with the data processing ([Degreane 2019](#)). It operates in a 5 beams and alternating low/high mode configuration. In the short to medium term, the low mode might be discarded. Its operational frequency is 1290 MHz, with corresponding wavelength of 0.232 m.

$$\lambda = \frac{c}{f} \tag{1.1}$$

with  $\lambda$  the wavelength in m,  $c = 299.79 \cdot 10^6 \text{ m s}^{-1}$  the speed of light and  $f = 1290 \cdot 10^6$  the frequency in Hz.

The wind profiler is oriented as shown in [Figure 1.1](#). The 55 altitudes of the gates are assigned to the center of the resolution volume. They are given in this report as normal to the ground (i.e. not radial, that is in the direction of the beam). They range from 299 to 8040 meters above ground level (AGL) in high mode (resolution of 144 m) and from 106 to 3202 meters AGL in low mode (resolution of 58 m).

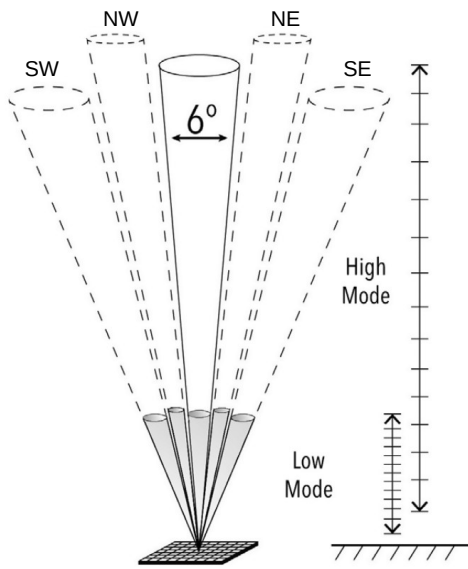


**Figure 1.1: Beam width and steering**  
Reprinted from [Weisshaupt et al. 2018](#)

The acquisition time for each beam, also called *dwell*, varies between 28 and 36 seconds. That means a complete cycle of 5 beams times 2 modes lasts for about 6 minutes. The start time of each dwell is provided to the user.

### 1.1.2 Measurement principle

The theoretical material supporting this section is based on the manual provided by [Scintec \(2016\)](#), another competitive company.

The wind profiler antenna emits electromagnetic waves as pulses into the air in a given direction. The shorter the pulse, the finer the spatial resolution. The waves can be scattered by non atmospheric targets such as trees, birds, airplanes or radio frequency interferences, and by two kinds of atmospheric targets: (1) hydrometeors, for instance rain and snow and (2) variations in the air refractive index. In the lower portion of the atmosphere, the latter depend on small scale temperature, pressure and humidity fluctuations stemming from turbulent eddies. The process is then called *Bragg scattering* and originates from irregularities about half the size of the wind profiler wavelength.

The Doppler shift is the frequency change a wave undergoes when being refracted by a moving object, relative to the wave source. The received frequency is higher if the object approaches the source and lower if it is receding. The radial Doppler frequency shift is directly proportional to the radial Doppler velocity shift of the object relative to the source. Radial means along the pointing direction of the beam.

$$f_r = \frac{-2 \cdot V_r}{\lambda} \quad (1.2)$$

with  $f_r$  the radial Doppler frequency shift in Hz,  $V_r$  the radial Doppler velocity shift in  $\text{m s}^{-1}$  and  $\lambda$  the wavelength in m.

If radial Doppler frequency shifts are to be compared between instruments having different operating frequencies, it is crucial to convert them to Doppler velocity shifts with the relevant wavelenght. [Table 1.1](#) gives conversion examples for the wind profiler PCL1300 (operating frequency 1290 MHz) with the aim of having an order of magnitude in mind.

**Table 1.1:** Conversion radial Doppler velocity/frequency shifts examples

Radial Doppler frequency shift	Hz	- 86.1	+ 10.0
Radial Doppler velocity shift	$\text{m s}^{-1}$	+ 10.0	- 1.16

### 1.1.3 Vertical motion

Clear air and hydrometeors reflectivities vary depending upon  $\lambda^{-\frac{1}{3}}$  (*Bragg scattering*) and  $\lambda^{-4}$  (*Rayleight scattering*) respectively. Hence wind profilers operating at great frequencies, or lower wavelength, are more sensitive to precipitation or clouds. The latter have an impact on the measurements, and more significantly in the vertical direction ([Doviak et al. 2006](#)).

A separation algorithm is proposed by [Radenz et al. \(2018\)](#) with the aim of removing the influence of falling particles from wind profiler Doppler spectra. They precise that clear air and hydrometeor scattering processes are independant and thus lead to the emergence of two distinct peaks in the spectrum. However, these peaks might be difficult to distinguish by traditional algorithms.

It is worth mentionning at this point that comparisons between wind profilers and rawinsondes measurements show standard deviations of about  $1.75$  to  $2 \text{ m s}^{-1}$  over a 3 years period. Those results are obtained for any kind of meteorological conditions but if bird migration periods are systematically excluded from the analysis ([Haefele et al. 2015](#)). Good agreement is also reported with another closely situated radar wind profiler ([Weber et al. 1990](#)), with tower ([Cohn et al. 2001a](#)) or aircraft ([Cohn et al. 2001b](#)) measurements and with a colocated Doppler lidar ([Mayor et al. 1997](#)).

## 1.2 Current signal processing

The current signal processing is summarized in [Figure 1.2](#). After a time domain averaging, the user receives a complex time serie which can be converted into a spectrogram with a Fast Fourier transform. A spectrogram is basically a collection of Doppler velocity spectra. The famous Merritt's algorithm is intended to filter contaminated spectra before performing an average over the 30 seconds acquisition time. It results in one average spectrum for each dwell. Spectrum peaks are identified, filtered and one is

chosen as the most likely due to the wind. The radial Doppler frequency shifts of those chosen peaks are averaged over 60 minutes approximately with a 10-minute update. Eventually, the wind velocity vectors  $u_x$ ,  $u_y$  and  $u_z$  can be calculated ([Degreane 2018a](#); [Degreane 2018b](#); documentation version T398050S matching the PCL1300 processing computer in Payerne in 2020).

### 1.2.1 Merritt's algorithm

A collection of Doppler velocity spectra (also called a spectrogram) is usually averaged over the dwell with the aim of reducing noise fluctuations. By doing so, contaminated spectra also contaminate the average. The problem is that they account for the major part of the signal as birds have stronger echoes than atmospheric signals (see [section 1.3](#)).

Merritt's algorithm, the first sucessful attempt to reduce bird contamination, identifies and separates signals stemming from different objects before performing the average. For noise and atmospheric signals, the real and imaginary parts (also refered to as  $I$  and  $Q$ ) of the timeserie are zero-mean Gaussian random variables and so the power ( $I^2 + Q^2$ ) is exponentially distributed. Rather, point targets show a power constant over short time intervals, non-exponentially distributed.

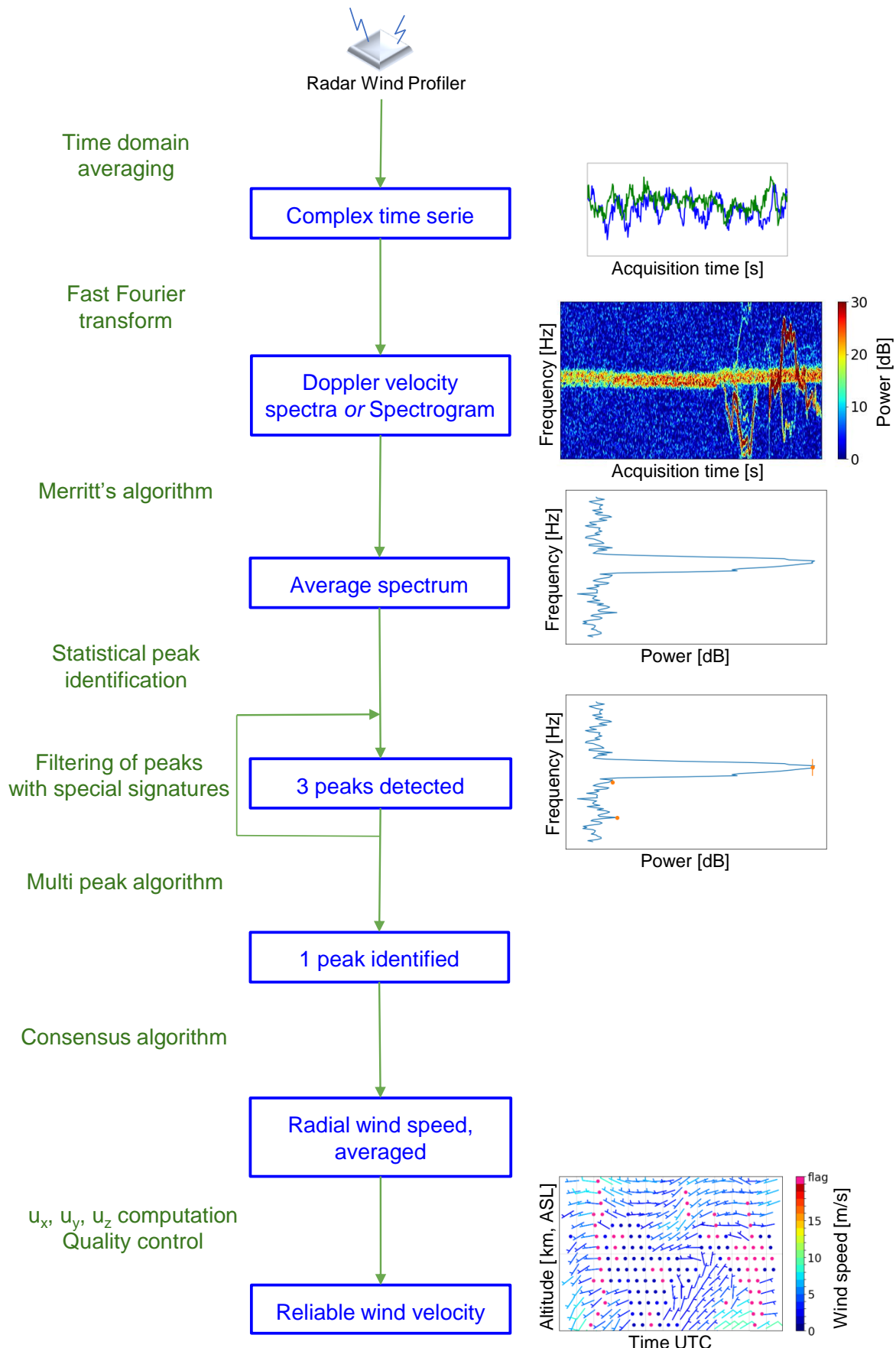
The algorithm computes  $\frac{\sigma^2}{\mu^2}$ , with  $\sigma$  the standard deviation and  $\mu$  the mean, within  $n$  frequency bins of  $M$  Doppler velocity spectra. It discards the ratios greater than 1, based on the Gaussian statistical test of [Hildebrand et al. \(1974\)](#).

There are several limitations to the method. First, higher order statistical moments should also be tested to ensure a Gaussian distribution. Second, noise and signals from clear air, precipitation and clouds are all Gaussian distributed according to the central theorem, since originating from a large number of sources. The algorithm does not differenciate them. Enventually, low level of contamination also produce weak signals that will not be discarded ([Merritt 1995](#)).

### 1.2.2 Statistical peak identification

Each average spectrum is divided into multiple regions statistically. Peaks with special signatures (ground clutter, radio frequency interference, point target) are filtered and 3 of the remainings are selected ([Degreane 2018b](#)).

The moments of those 3 detected peaks are estimated after substracting the noise contribution to the spectrum: (0<sup>th</sup>) total area of the signal spectrum gives the power, (1<sup>st</sup>) Doppler frequency shift, (2<sup>nd</sup>) spectral width, that is the square root of the velocity variance and (3<sup>rd</sup>) skewness accounting for the assymetry of the peak.

**Figure 1.2: Current signal processing flowchart**

Note that the word spectrum is singular, when a spectra refers to a collection of several spectrum

### 1.2.3 Multipeak and consensus algorithms, quality controls

A fuzzy logic with Gaussian penalty functions is applied to identify the peak that is most probably due to clear air. Each of the 3 peaks previously detected obtains a score, depending on various spatial/temporal continuity criteria on velocity, spectral width and power level. For complementary informations, see [Cormann et al. \(1998\)](#). The peak with the highest score is fed to the consensus algorithm.

The latter implements a sliding window whose position maximises the number of measurements. The output is an average of the Doppler frequency shifts associated to the identified peaks within the optimal window. If there are not enough measurements within the window, the average is not considered as representative and thus rejected. A value can also be discarded if the signal to noise ratio is too weak ([Degreane 2018b](#)).

The average is performed over 60 minutes approximately on the basis of a 10-minute update. The assumption is homogeneity in the wind field over the spatial separation of the beams and is reasonable in a stable atmosphere. However, that assumption is violated in highly localized convective conditions. Averaging over a sufficient period of time compensates for atmospheric instability ([Scintec 2016](#)).

A quality control based on T- and F- tests applied to various signal statistics henceforth allows to consider the average as a reliable wind estimate. Failure of the tests will result in the absence of data ([Degreane 2018b](#)).

### 1.2.4 Wind vector calculation

The average Doppler frequency shift coming from the consensus algorithm can be converted into radial velocity, measured in the direction of the beam. The vertical beam and at least two opposite oblique beams are needed to further compute the wind velocity vectors  $u_x$ ,  $u_y$  and  $u_z$  ([World Meteorological Organization 2018](#)).

$$\begin{aligned} u_x &= - \left( \frac{V_{rx} - V_{rz} \cdot \sin \theta_x}{\cos \theta_x} \right) \cdot \sin \phi_x - \left( \frac{V_{ry} - V_{rz} \cdot \sin \theta_y}{\cos \theta_y} \right) \cdot \sin \phi_y \\ u_y &= - \left( \frac{V_{rx} - V_{rz} \cdot \sin \theta_x}{\cos \theta_x} \right) \cdot \cos \phi_x - \left( \frac{V_{ry} - V_{rz} \cdot \sin \theta_y}{\cos \theta_y} \right) \cdot \cos \phi_y \\ u_z &= -V_{rz} \end{aligned} \quad (1.3)$$

with  $V_{rx}$  and  $V_{ry}$  being the average radial Doppler velocity shifts of the two opposite oblique beams chosen (identified with subscripts  $x$  and  $y$ ),  $V_{rz}$  the average radial Doppler velocity shift of the vertical beam,  $\theta_x$  and  $\theta_y$  the elevation angles of the two oblique beams equal to  $15^\circ$  ( $0^\circ$  is vertical),  $\phi_x$  and  $\phi_y$  the azimuths of the two oblique beams ( $0^\circ$  is North). All angles have to be converted to radians.

If radial Doppler velocity shifts are to be obtained from the wind velocity vectors, the equations are the followings:

$$\begin{aligned} V_{rx} &= u_x \cdot \sin \theta_x \cdot \sin \phi_x + u_y \cdot \sin \theta_x \cdot \sin \phi_x + u_z \cdot \sin \theta_x \\ V_{ry} &= u_x \cdot \sin \theta_y \cdot \sin \phi_y + u_y \cdot \sin \theta_y \cdot \sin \phi_y + u_z \cdot \sin \theta_y \\ V_{rz} &= -u_z \end{aligned} \quad (1.4)$$

The wind vectors can still be "flagged" at this final stage if the calculated wind vectors are not consistent accross beam pairs ([Degreane 2018b](#)).

## 1.3 Bird contamination

Many bird species gather in large flocks during migration, which occurs from February until June with a maximum in April and from July until November with a maximum in September. Spring and autumn migrations are characterized by southward and northward flights respectively, at the level of most favorable winds (2 to 4 km) and during night time only, avoiding cloud and rain. [Wilczak et al. \(1995\)](#) reports up to 64% of contaminated nights over 17 stations spread accross the US for the months of March, April and May 1993.

The birds average speed of 8 to 15  $\text{km s}^{-1}$  results in the same range of errors in wind speed measurements. It is also common to observe barbs suddenly pointing out southerly or northerly depending on the season. Bird contaminated data reveal high signal power, their high water content turn them into strong reflectors, and large spectral widths. However, those can be associated with precipitation as well. In addition, peaks tend to show 3 modes if the dwell is longer than the wings flapping period ([Wilczak et al. 1995](#)).

The problem of bird contaminated wind profiler measurements is well known for about 25 years. It has been less addressed within the last decade as lidars gradually broke into the market. The differences between the both is discussed later in [section 2.3](#). Yet, as lidar beamwidths are much smaller, bird contamination constitutes less of a challenge.

[Merritt \(1995\)](#) and [Kretzschmar et al. \(2003\)](#) addressed the issue of bird contamination straight on spectrograms. On the other hand, ongoing research by [Lehmann \(2012\)](#) focuses on the transform applied to convert the time serie into a spectrogram. Both are briefly presented in the next subsections [1.3.1](#) and [1.3.2](#).

This work follows in the footstep of spectrograms post-processing. The recent development of computing power has encouraged its novelty, namely the use of the Convolutional Neural Network.

### 1.3.1 Classification of contaminated spectrum with Neural Networks

After Merritt's algorithm, a second attempt in reducing bird contamination is made by [Kretzschmar et al. \(2003\)](#) and [H. Weber \(2005\)](#). The data come from the wind profiler Radian LAP-3000 located in Payerne, supplemented by an infrared system having a smaller beam width. Contamination is considered as such only if the bird is detected on both instruments.

The approach uses Doppler velocity spectra before averaging on the dwell. The calculated moments of the identified peaks are fed to a neural network. If classified as contaminated, spectra are discarded. In a nutshell, the method is equivalent to Merritt's algorithm but uses Machine Learning instead of statistical distribution tests.

Two types of neural networks are tested, a FFNN and a QNN. The first one results in a hard classification (assignment of the sample to only one class) when the second one uses a multilevel activation function allowing a soft classification. The effort focuses on optimizing the size of the network and the features used, that are the followings ultimately:

1. Signal power, the birds having a high reflectivity as aforementioned
2. Spectral width as bird contaminated peaks tend to be larger
3. Skewness and kurtosis, that revealed being primordial to a good performance
4. Time and height averaged signal power variances
5. Time and height relative signal power difference, as the echoes are of short duration and propagate on several gates
6. Skewness and kurtosis time averages
7. Vertical gate spacing, width and height, characterizing the operational mode

[Kretzschmar et al. \(2003\)](#) reports a hit rate for birds of 97.2 %. The false alarm rates associated to clear air and rain are of 3.3/0.9 % and of 0.7/28.4 % in high and low mode respectively. The hit rate is equivalent to the recall and the false alarm rate is also known as the false positive rate.

$$\text{recall} = \frac{TP}{TP + FN} \quad \text{false positive rate} = \frac{FP}{FP + FN} \quad (1.5)$$

with TP the true positive, FN the false negative and FP the false positive.

### 1.3.2 Gabor filtering algorithm

[Lehmann et al. \(2008\)](#) emphasise the necessity to deal with bird contamination before computing the spectrogram. To do so, they suggest the use of a Gabor transform, in continuity with the approach suggested by [Jordan et al. \(1997\)](#) which is often referred to as the wavelet-based method.

A Gabor transform is a special windowed short-time Fourier transform. A Fourier transform reveals good resolution in the frequency domain but is generally inadequate for non-stationary signals as information on time dependency is lost. The bird clutter contribution to the signal can be highly non-stationary. Windowing the function to be transformed by multiplying it by a Gaussian function addresses this issue at the cost of a reduced frequency resolution ([Gabor 1946](#)).

One should bear in mind the difference between a Gabor transform and the Gabor filtering algorithm introduced by [Lehmann et al. \(2008\)](#). Naturally, the latter implies a Gabor transform but also discards the contaminated Gabor coefficients thus eliminating the clutter component of the raw signal. Based on Merritt's findings, the method applies the Gaussian statistical test of [Hildebrand et al. \(1974\)](#) to the squared modulus of the Gabor phase space coefficients for fixed frequency bins.

The algorithm is further optimized in [Lehmann \(2012\)](#) with subsequent quality controls. As with Merritt's algorithm, there is a critical bird density beyond which the chances for a clear-air atmospheric echo retrieval are limited.

## 2 Dataset

The data come from the wind profiler and from a Doppler lidar. The idea is to perform a classification of the spectrograms issued from the wind profiler, thus excluding those where the wind is not visible either because the signal is too low or because bird contamination is too heavy. The lidar radial Doppler frequency shift is then used as target on the exploitable spectrograms.

In this section, you will find a description of the various sources composing the dataset along with their visualisation and a reminder of their position in the current processing chain ([Figure 1.2](#)). After a description of the lidar key operational aspects, the coherency between wind profiler and lidar measurements is evaluated to the extend required to make use of it consistently.

### 2.1 Description

The dataset begins on June 19 and ends on August 18, 2020 with a total of 40 days of sunshine and 20 days where it rained at least once. 7 days are missing in this period as the radar had to be turned off for technical reasons. High mode is exclusively considered, it is the one that will be maintained in the long run. Every single clear night shows bird contamination, whereas its intensity varies according to the date.

#### 2.1.1 Data sources

For the sake of clarity, an exhaustive list of available data with additional details is built below:

1. Wind profiler time serie (raw data)
2. Wind profiler spectrograms, computed from the time serie with a discrete Gabor transform ([LFAT 2020](#), function *dgt, discrete Gabor transform*). However, no filtering of any kind is carried out.
3. Wind profiler average spectra for each dwell along with the estimated spectral moments for the 3 selected peaks, i.e. radial Doppler frequency shift, width, skewness and signal level. One noise value is given per average spectra. Referring to the current processing flowchart, peaks with special signatures have been discarded at that point. It is particularly noticeable with respect to the ground clutter. However, the subsequent multipeak, consensus algorithms and quality control have not been applied yet. It is thus very likely that there will be systematic

inconsistencies in the data. Moreover, the peak which will be further chosen remains unknown.

4. Wind profiler output product, that is  $u_x$ ,  $u_y$  and  $u_z$  on a 60 minutes average with a 10-minute update at each measured altitude. Flagged values come from incoherent wind vectors across beam pairs, while missing values result from failed quality control tests. To obtain a radial Doppler frequency shift, [Equation 1.4](#) is used.
5. Lidar radial Doppler velocity shifts, converted to Doppler frequency shifts with the wind profiler wavelength of 0.232 m ([Equation 1.1](#)). Those come along with a possible flag as well.

### 2.1.2 Visualisation

A few key features are presented in [Figure 2.1](#). Bird contamination is visible from midnight to 5am UTC. Many values are flagged meaning that measurements were not coherent across beam pairs. On other days, it can appear in the form of missing data which failed quality control tests. Rain is measured on the ground from 7:40pm (19:40) UTC to midnight, thus inducing flagged values displayed as pink dots. The rain event is accompanied by stronger north-easterly winds.

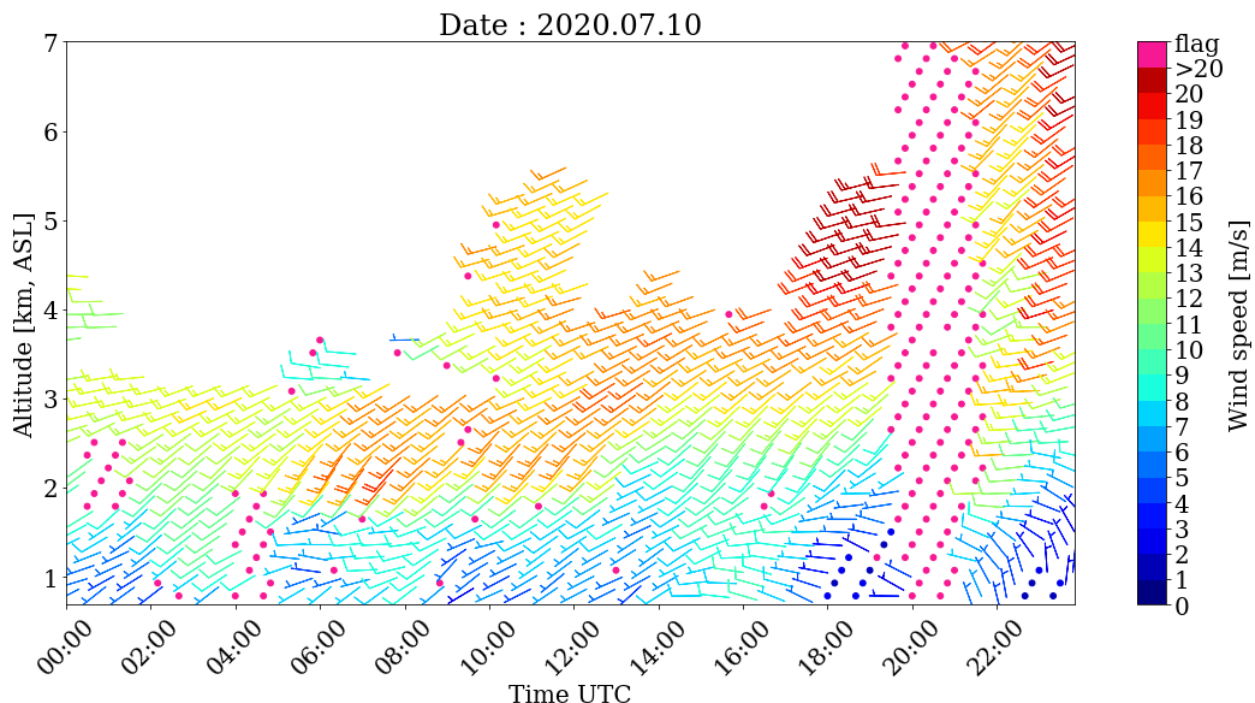


**Figure 2.1: Wind field on July 10, 2020 (high mode)**

Sunset is approximately at 8pm (20:00) UTC and sunrise at 4am UTC (Central European Summer Time : UTC + 2 hours). Bars are obtained on a 10-minute update (one out of 4 displayed) and plotted at the end of the 10 minutes.

Even though the contamination was verified on spectrograms, [Figure 2.2](#) validates the statement. The power appears higher from 00:00 to 04:00 am UTC in the presence of birds as mentionned in [section 1.3](#). Hydrometeors also show high reflectivity. The significant values at low altitudes from 06:00 am to 04:00 pm are presumably coming from evapotranspiration.

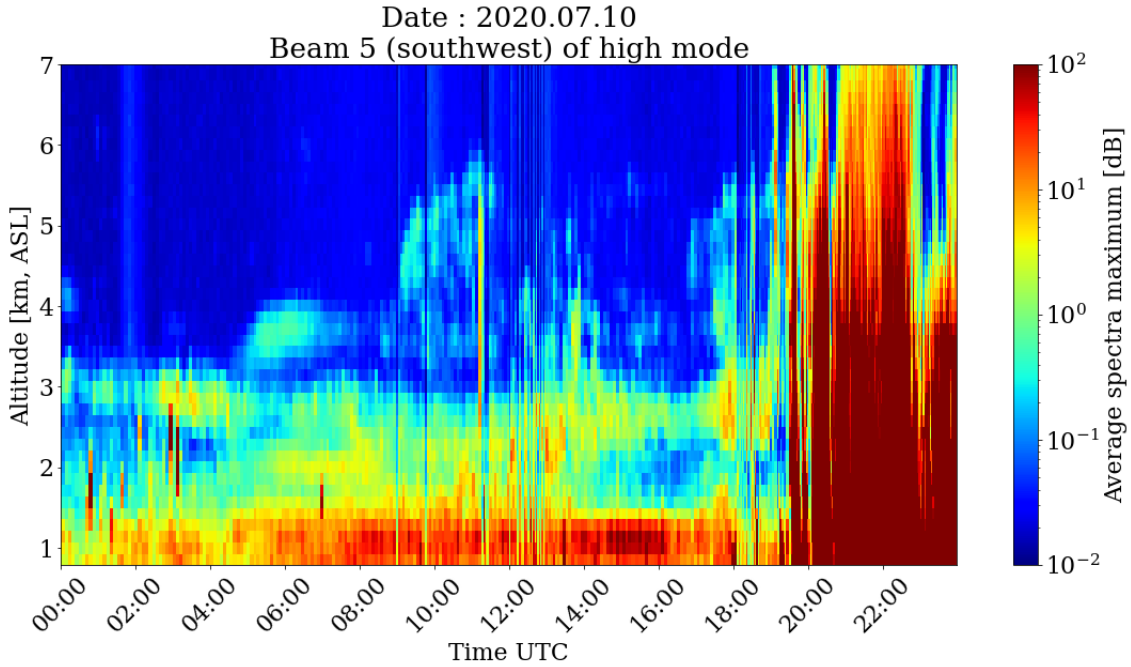


**Figure 2.2: Maximum power of average spectra** for each gate altitude and over time, in one direction. Ground-based measurements indicate continuous rain from 7:40 pm (19:40) UTC until midnight

The dataset components simultaneous visualisation is possible on [Figure 2.3](#) on the 25<sup>th</sup> of June of 2020 (one gate, one beam). From 03:21 to 03:33 am UTC, spectrograms are clear from any contamination except the ground clutter (1<sup>st</sup> line). The average spectra shows a single sharp peak, note the small offset in the detection of the peak though (2<sup>nd</sup> line). The amplitude of the timeserie is small (3<sup>rd</sup> line). As there was a lot of contamination within the previous 60 minutes, wind vectors are flagged (4<sup>th</sup> line).

Times 02:16 (first spectrogram), 03:03 and 03:15 are considered as heavily contaminated: the wind is not visible anymore, completely covered by the bird clutter. The time serie shows a larger amplitude. At 02:16, the average spectra does not present an identifiable peak. At 03:15, it does but its position is incorrect. Eventually 02:52, 02:58 and 03:09 would be considered as slightly contaminated as the wind is still apparent.

The challenge lies in determining the class of cases at 02:22 and 02:46 am UTC: is the wind still visible to the human eye ? Other interesting examples are presented in [Appendix A](#). Those cases are not seldom and might be encountered on a regular basis.

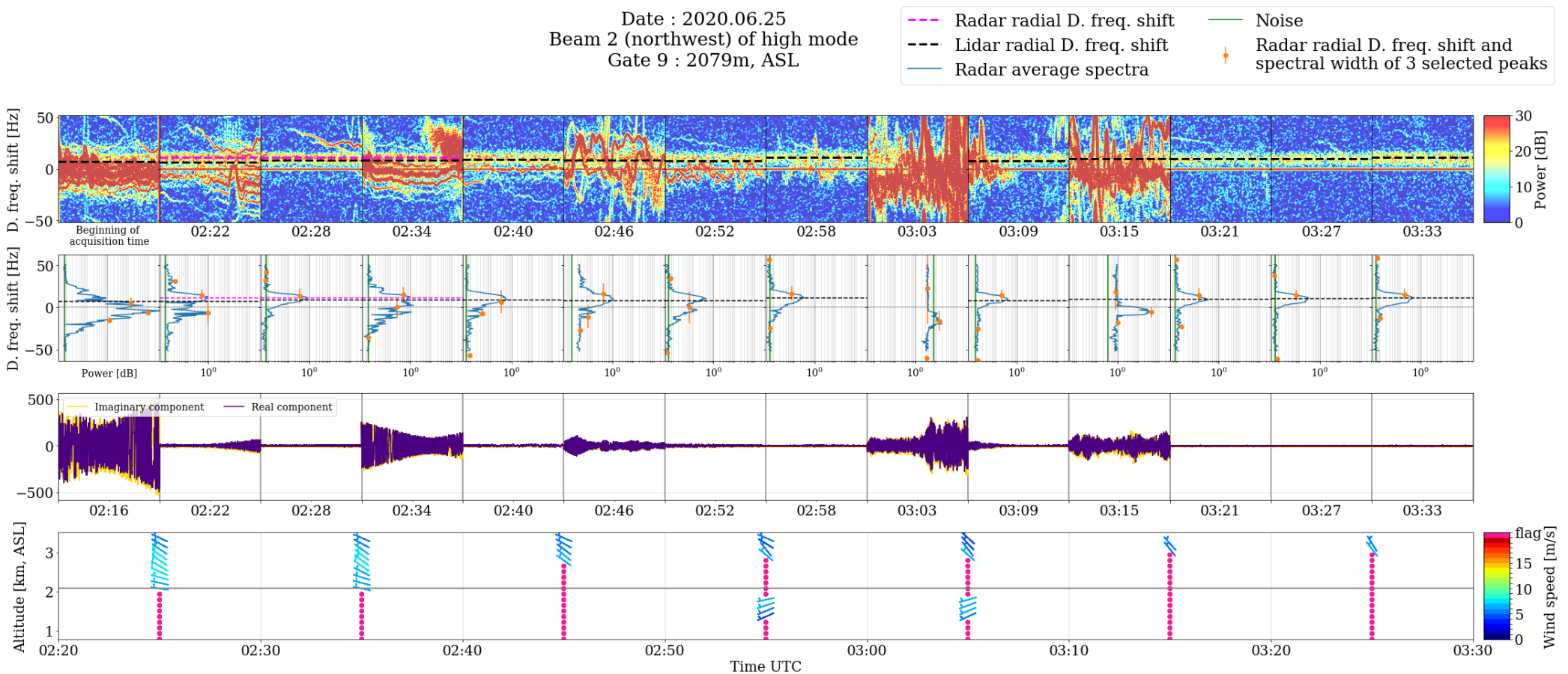


**Figure 2.3: Viewing of the dataset available including all data sources**

- 1<sup>st</sup> line : wind profiler spectrograms computed from the time serie with a discrete Gabor transform
  - 2<sup>nd</sup> line : average spectra for each dwell with selected peaks and associated moments
  - 3<sup>rd</sup> line : time serie (raw data)
  - 4<sup>th</sup> line : wind barbs, displayed between the 10 minutes for better visualisation
- Note: As aforementioned, the radar radial Doppler shifts come from an average

### 2.1.3 Disk space considerations

The dataset pre-processing pipeline required a significant amount of time and work. Indeed, the needed functions are written in Matlab but Python is chosen to perform Machine Learning for flexibility reasons.

The wind profiler time series are stored in a format which can be read using C++. A day of data in that format weights about 2 to 3 GB. The functions allowing its retrieval and computing the spectrograms are numerous. They are not available in Python and could not be re-written.

The first attempt was saving the spectrograms as netCDFs to be able to read them in Python. That was equivalent to roughly 250 GB of data per day if working with all beams, gates and modes. On a 4 cores regular laptop, it needed far more than a day to be produced. Substantial efforts were needed to reduce the computational time and to be able to save more than a few days on the disk space available.

The implemented optimisation makes use of the so-called Matlab engine ([MATLAB & Simulink 2020](#)) allowing the direct retrieval of the Matlab function output in a Python shell. The spectrograms are then saved as tensors within a format called TFRecords [TensorFlow Core - TFRecord 2020](#).

First of all, an intermediate data storage is needed as the whole dataset does not fit in the RAM. TFRecord is the recommended format by Python as it enables faster training ([TensorFlow Core - Better performance 2020](#)). Moreover, only the necessary data is saved which considerably reduces its size. Eventually, besides disk space, considerable time is gained in uploading/downloading tasks.

## 2.2 Doppler wind lidar

### 2.2.1 Operational informations

The mobile lidar is a Windcube, model 100S provided by Leosphere. Two datasets are acquired in Payerne: (1<sup>th</sup>) covering the month of June 2019 with a northward orientation and (2<sup>nd</sup>) from June 18, 2020 onwards. During that second period, the lidar is configured with a 315° offset, which means that radar and lidar beams are aligned as presented in [Table 2.1](#). In addition, both instruments are located a few meters away from one another.

Its operation during the first 6 minutes of each hour is configured as fixed, in order to obtain at least one full overlap of both instruments acquisition times. The fixed measurements are performed on oblique beams exclusively.

**Table 2.1:** Radar/lidar beams correpondance, as of July 2020

Azimuth [°]	vertical	315	135	45	225
Orientation	vertical	northwest	southeast	northeast	southwest
Radar beam number	1	2	3	4	5
Lidar beam number	5	1	3	2	4

The lidar provides the user with the end of the acquisition time. On average, there are time lapses of 8.3 and 5.8 seconds for oblique and vertical beams respectively. As aforementioned, the radar dwells vary between 28 and 36 seconds and the start time is given. Radar measurements are performed diagonally in order to minimize the time period between two opposite beams.

Unlike radar wind profilers, the laser pulse emitted by the lidar at different heights is scattered back by atmospheric aerosols travelling with the wind. The Doppler shift induced by their motion remains as described in [subsection 1.1.2](#). Additionally, a Doppler lidar does not operate during precipitation events.

There will be no further consideration on the technical details of the lidar measurement principle as its output is only exploited (see [World Meteorological Organization \(2018\)](#) for more details).

## 2.2.2 Measurements pairing

The lidar gates altitudes range from 200 to 12000 m (normal distance to the ground, AGL) with a resolution of 100 m. A linear interpolation on the lidar Doppler frequency shift is used to match the wind profiler gate altitudes. The minimum, maximum and mean differences between radar and lidar gate altitudes are displayed in [Table 2.2](#).

Concerning the temporal resolution (excluding the first 6 minutes), one would come accross 3 specific cases: (1) there is one lidar acquisition time included within the ~30 seconds radar acquisition, (2) if there are several lidar acquisition times included within the ~30 seconds radar acquisition, an average is performed and (3) there is no overlap between the two measurements, the closest lidar acquisition time is held.

**Table 2.2:** Altitudes differences, as of July 2020

	Minimal difference [m]	Maximal difference [m]	Mean difference [m]
High mode	0	50	24.9
Low mode	1	94	26.2

### 2.2.3 Resolution volumes

The lidar beam width is a few tenths of centimeters. The radar aperture of  $6^\circ$  leads to a width of 30 m at a height of 300 m above ground and of about 840 m at 8000 m. The volumes of resolution are different for both instruments, size and location-wise.

However, they are not taken into account in the framework of the thesis. This choice is made based on [Cohn et al. \(2002\)](#) considerations who performed a comparison between Doppler lidar and radar measurements without accounting for the contribution of each sampling volume to the total observed standard deviations.

Both instruments were 25 meters apart in the study, with the lidar sampling volume lying within the radar volume. The measurements were coincident in time. Although the radar volume is several order of magnitude greater, their justification lies in the fact that advection of the atmosphere through it over a 25 seconds dwell reduces the difference to only 3 orders of magnitude.

On data free from ground clutter contamination or interferences and presenting a good signal-to-noise ratio, they report a  $R^2$  of 0.99. Standard deviations were about 0.20-0.23 and  $0.16\text{-}0.35 \text{ m s}^{-1}$  for radial velocities higher and lower than  $1 \text{ m s}^{-1}$  respectively. A standard deviation of  $0.23 \text{ m s}^{-1}$  reflects an error in horizontal wind of less than  $1 \text{ m s}^{-1}$  for one cycle and of  $0.11\text{-}0.27 \text{ m s}^{-1}$  on a 30-minute average.

## 2.3 Coherency evaluation

The correlation between radar and lidar measurements from June 19 to August 18, 2020 is assessed in terms of  $R^2$  and Mean Absolute Error (MAE). Different filters listed in [Table 2.3](#) are established in order to quantify the influence of precipitation, bird contamination, temporal and spatial resolutions. The more filters there are, the smaller the number of samples become.

**Table 2.3:** Description of the different filters implemented

Scenario	Mean number of samples (rounded)	Scenario definition
M1	First moment (assumption : highest)	250 661
MClose	Closest moment to the lidar value	250 661
	<i>For the next scenarios, the closest velocity shift to the lidar value is always picked</i>	
Sun	40 days of sunshine	135 071
Rain	20 rainy days (rained at least once)	111 406
Day	Daytime hours, sunrise at 4 UTC (July 2020)	179 321
Night	Nighttime hours, sunset at 20 UTC (July 2020)	71 339
SNR 3	Radar signal-to-noise ratio higher than 3 dB	237 090
Best	MClose + Sun + Day + SNR 3	92 237
MClose Gate 7	Gate 7, 1303 meters AGL	13 132
Fixed	6-minute stare at the beginning of each hour	8 433
Fixed Gate 7	Fixed at altitude 1303 meters AGL	407

Radar measurements are the radial Doppler velocity shifts of the 3 detected peaks stemming from the wind profiler average spectra. This is before any subsequent filtering algorithms (see [subsection 2.1.1](#)). There is no information given at that point in the files on which of the 3 peaks is/will be picked.

The first scenario *M1* assumes a selection of the first value provided, presumably the highest. A second attempt *MClose* favors the peak whose value is the closest to the lidar Doppler velocity shift. As it turns out to be the best way of proceeding, the method is kept for the following scenarios.

There seems no other way forward. Reprocessing the data on a time-scale equal to the dwell would provide the user with the required information. It has been tried but was unsuccessful on such a small time-scale.

### 2.3.1 Precipitation and bird contamination

The  $R^2$  and MAE of the first 8 scenarios are presented in [Figure 2.4](#). Some of the associated scatter plots are displayed in Figures [2.6](#) and [2.5](#), with the radar measurements on the x-axis and the lidar measurements on the y-axis.

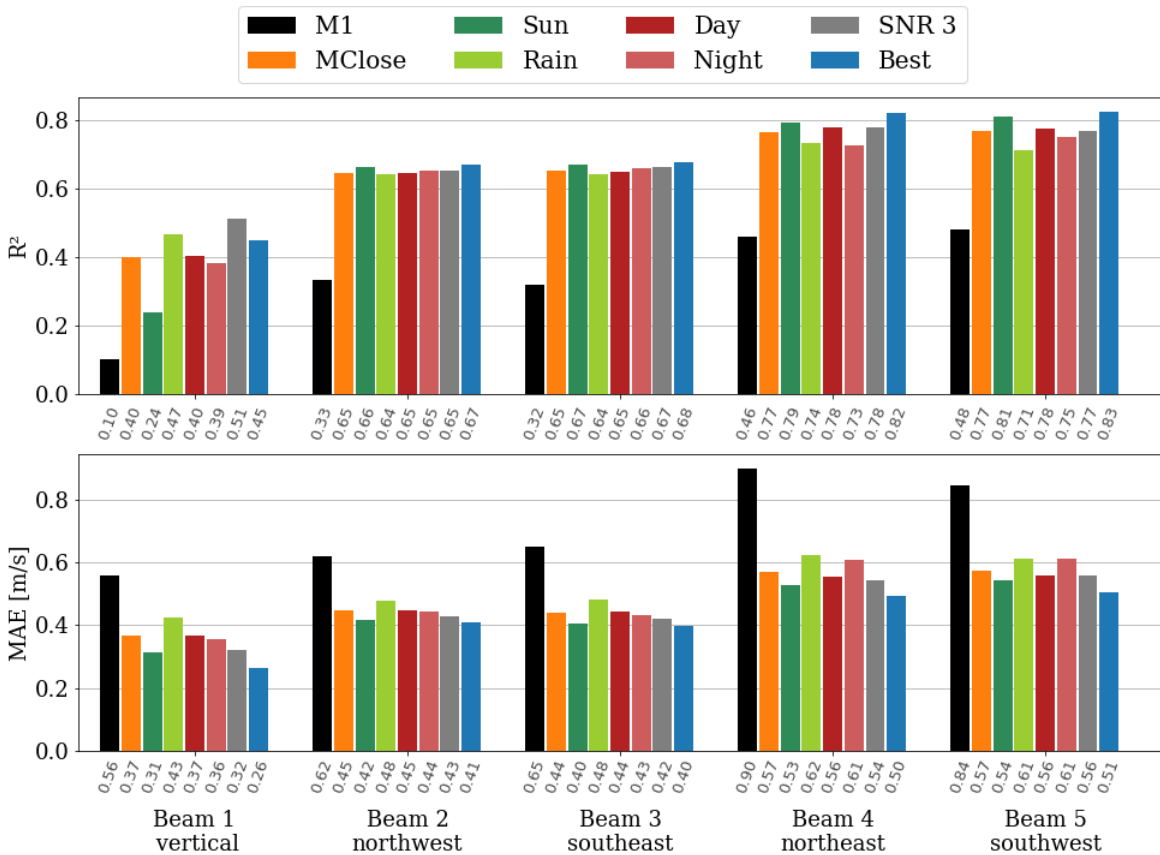


**Figure 2.4: Radar/lidar correlations per beam from June 19 to August 18, 2020**

First 8 scenarios presented in [Table 2.3](#)

Picking the closest Doppler velocity shift to the lidar value increases the  $R^2$  of at least 0.2 for all beams and decreases the MAE significantly as well. As mentioned, the method is applied to the following scenarios:

1. **Sun and rain:** For oblique beams, the  $R^2$  increases and the MAE decreases on sunny days. It is most probably due to the bias induced in vertical velocity by drops or clouds. The tendency is always similar, an increase in  $R^2$  between two opposite scenarios leads to a decrease in MAE and vice versa.

- 2. Day and night:** Beam number 1, 4 and 5 show a lower  $R^2$  during the night, the difference might be due to bird contamination as expected. However, the other beams indicate no substantial differences.
- 3. SNR:** To compute the signal-to-noise ratio, the signal level of the closest peak to the lidar measurement is selected along with the single noise value provided for each average spectra. A threshold on the SNR is fixed to 3 dB, which is the one inducing a clear improvement.
- 4. Best:** Filtering nighttime hours, rainy days and signal-to-noise ratio leads to the best results in terms of  $R^2$ , about 0.67 for beams 2 and 3 and 0.82 for beams 4 and 5. Interestingly, the MAE is always lower for beams 2 and 3. Looking at the scatter plots, it is due to the spread of the measurements. Furthermore, north-easterly and south-westerly winds were prevalent during the assessed period.

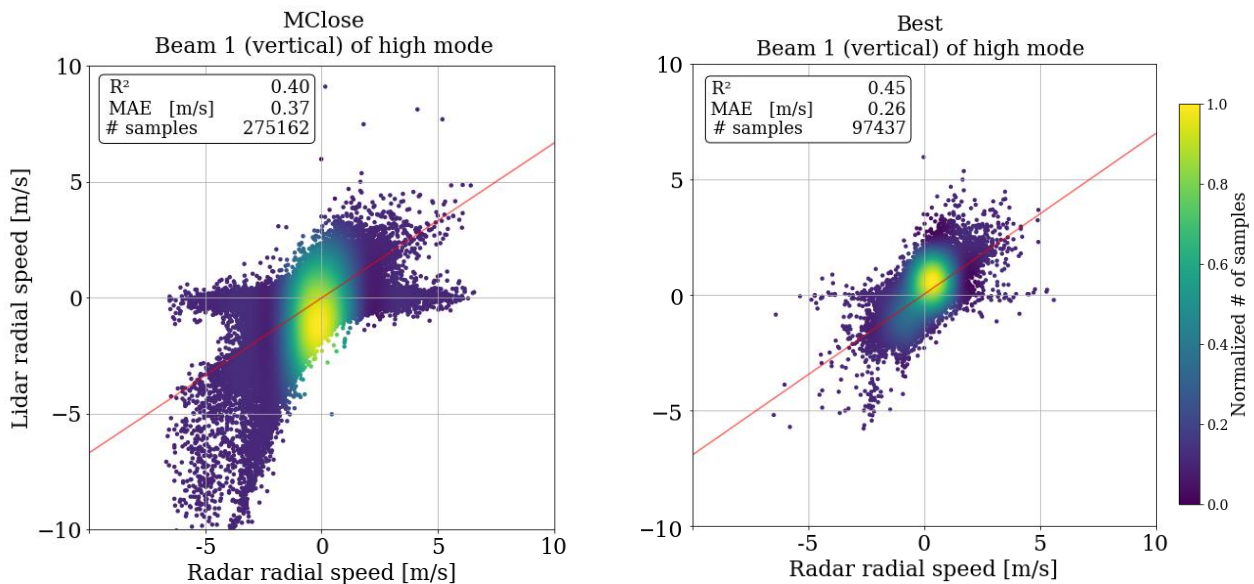


**Figure 2.5: Vertical beam of high mode from June 19 to August 18, 2020**  
**MCclose (left) and Best (right), the red line being the regression line**

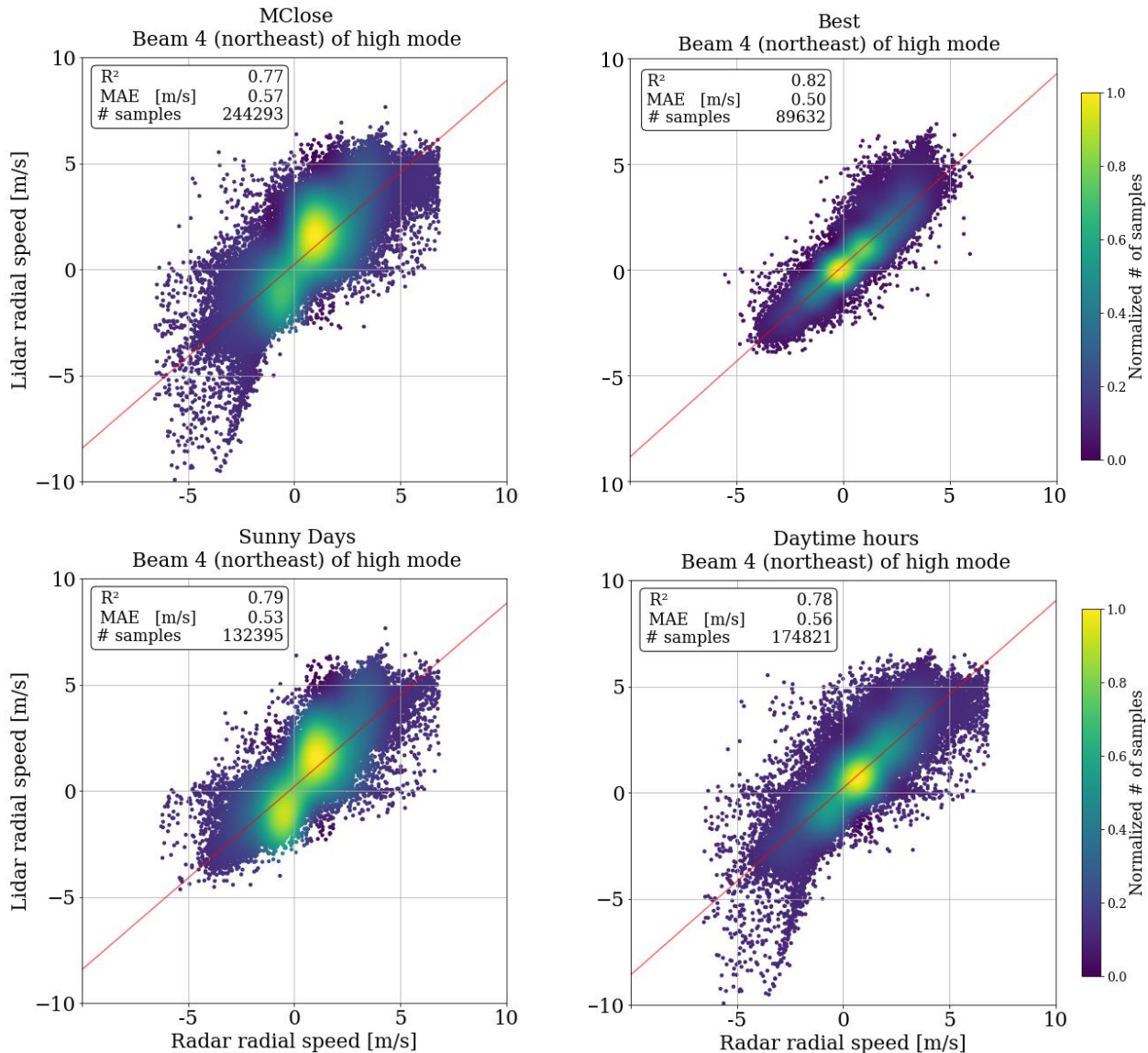


**Figure 2.6: Northeasterly beam of high mode from June 19 to August 18, 2020**

MCclose (upper left), Best (upper right), Sun (lower left) and Day (lower right)  
The red line is the regression line

### 2.3.2 Temporal and spatial resolutions

The 6-minute stare at the beginning of each hour can be a way to quantify the influence of the time gap between both instruments. Additionally, gate number 7 is favoured as

located 1303 meters above ground level. The altitude difference to the lidar gate is of 3 meters only.

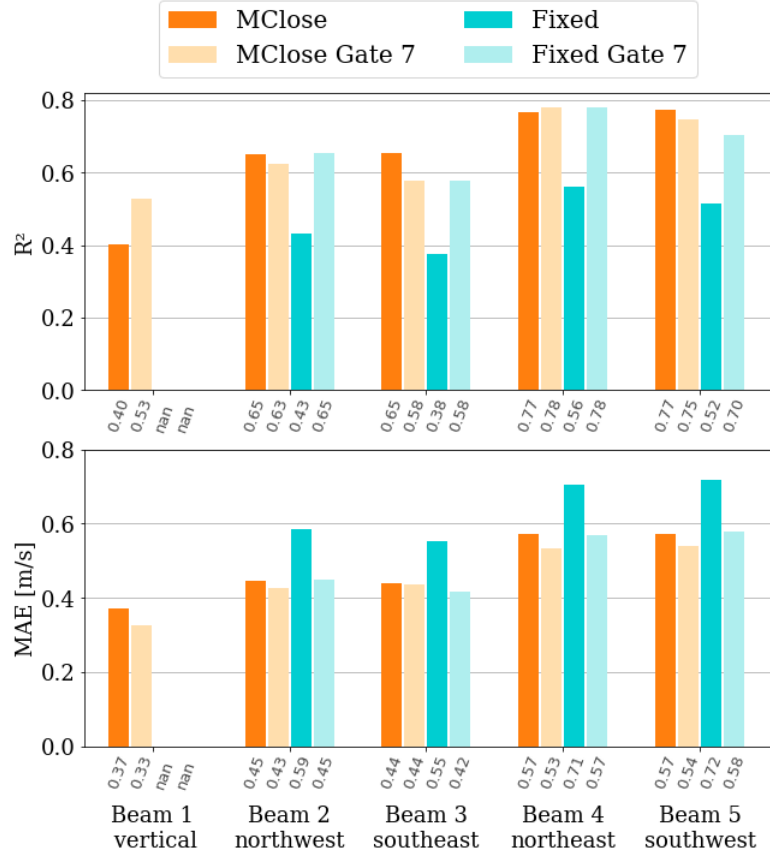


**Figure 2.7: Temporal and spatial resolutions influence on the radar/lidar correlations from June 19 to August 18, 2020**

Last 3 scenarios presented in [Table 2.3](#), with MCclose as additional reference

When selecting gate number 7, [Figure 2.7](#) does not show any overwhelming improvement in  $R^2$  except for the vertical beam. It leads to the conclusion that gates spatial distribution is more of an issue in the vertical direction. However, it diminishes the MAE for all beams. The reason is the same as mentioned earlier, the spread is reduced to a great extend ([Figure 2.8](#), upper right).

The 6-minute stare produces a great decrease in  $R^2$  and a systematic increase of the MAE when all gates are considered. When gate number 7 is held, results are approximately comparable to scenario *MCclose*.

The interpretation is uncertain. One might keep in mind that the number of samples is

highly reduced in those cases. The scatter plots of Figure 2.8 (lower left and right) seem to outline a high concentration of points around 0.

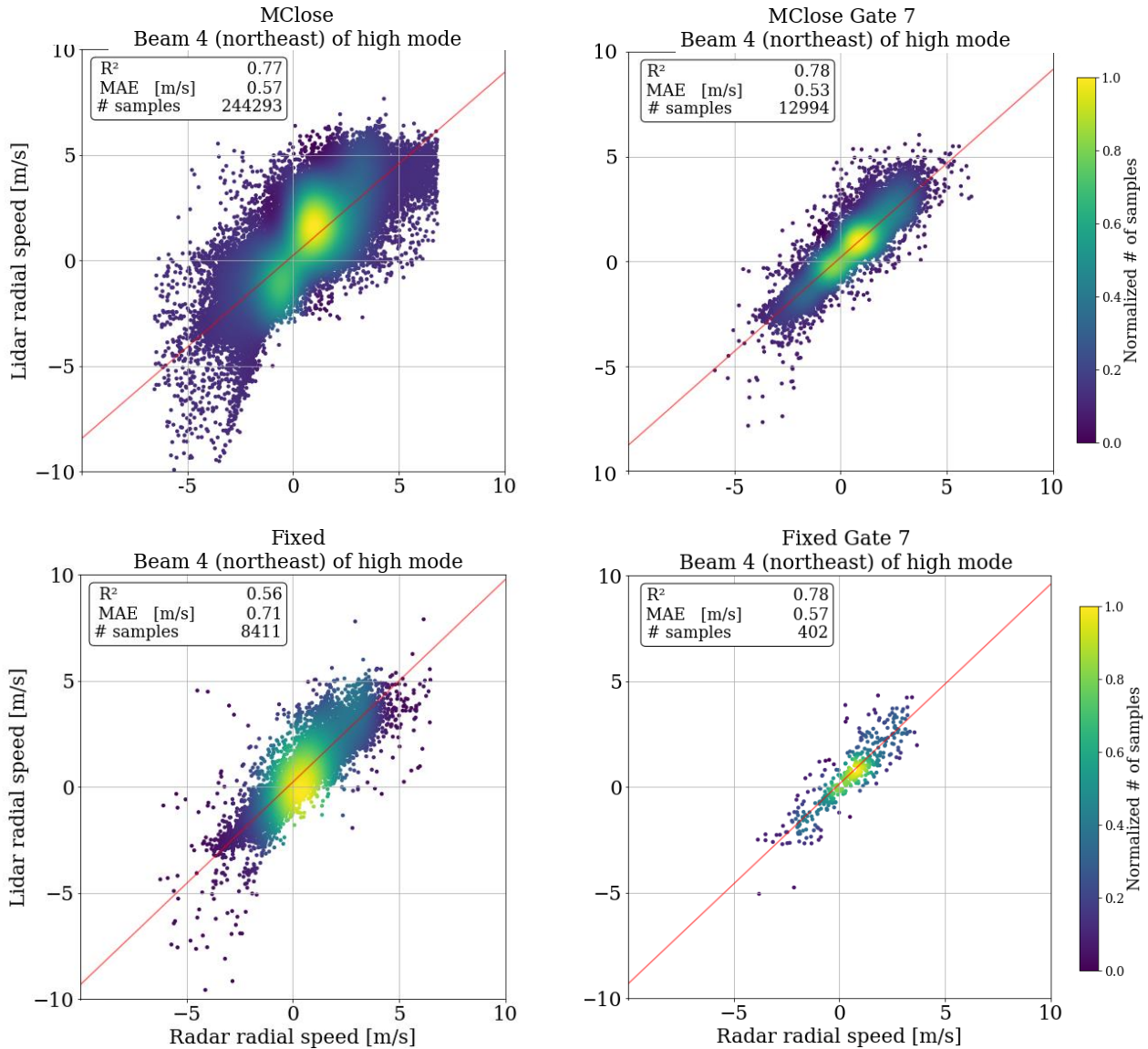


**Figure 2.8: Northeasterly beam of high mode from June 19 to August 18, 2020**  
MCclose (upper left), MCclose Gate 7 (upper right), Fixed (lower left), Fixed Gate 7 (lower right), the red line being the regression line

# 3 Models and methods

The section starts with a split of the spectrograms in 4 classes : (0) no visible wind, (1) visible wind only, (2) massive bird contamination and (3) slight contamination and wind still visible. A second stage focuses on predicting the Doppler frequency shift of samples belonging to classes 1 and 3.

All codes are available at <https://github.com/MaL-R/RWP>. A fuller description of the TensorFlow models can be found in the [Appendix B](#). Spectrograms in train, validation and test sets can be appreciated at [https://github.com/MaL-R/RWP\\_spectrograms](https://github.com/MaL-R/RWP_spectrograms).

## 3.1 Classification

### 3.1.1 Manual classification tool

A graphical interface is set up with a package called Tkinter to speed up the manual classification task. The entirety of the dataset is displayed within the self-opening window ([Figure 3.1](#)). The wind barbs and time serie help to better determine the class. Rain is automatically flagged and assigned to number 4 based on ground measurements. A last class 5 can be employed in case of doubts or when the lidar value is not coherent.

The possibility to move forward to a specific gate number included between 0 and 54 is offered. The choice needs to be saved with *Ctrl-s* (keep *Ctrl* pressed down before pushing *s*). Fields dedicated to classes only accept numbers from 0 to 5 and would not allow being left empty. If the specific spectrogram has already been classified, the value will appear in the fields when the window opens. Closing the window is possible with a *Ctrl-c* or its assigned button, once all fields are filled.

The tool jumps from one hour to the next one when pressing *Enter*. Once 24 hours have been completed, it goes to the next gate. Specific hours of the day can be selected as well as a distinct gate increment. For each day and each beam, the classification is stored in the form of a Panda dataframe with gate numbers as rows and measurement times in columns.

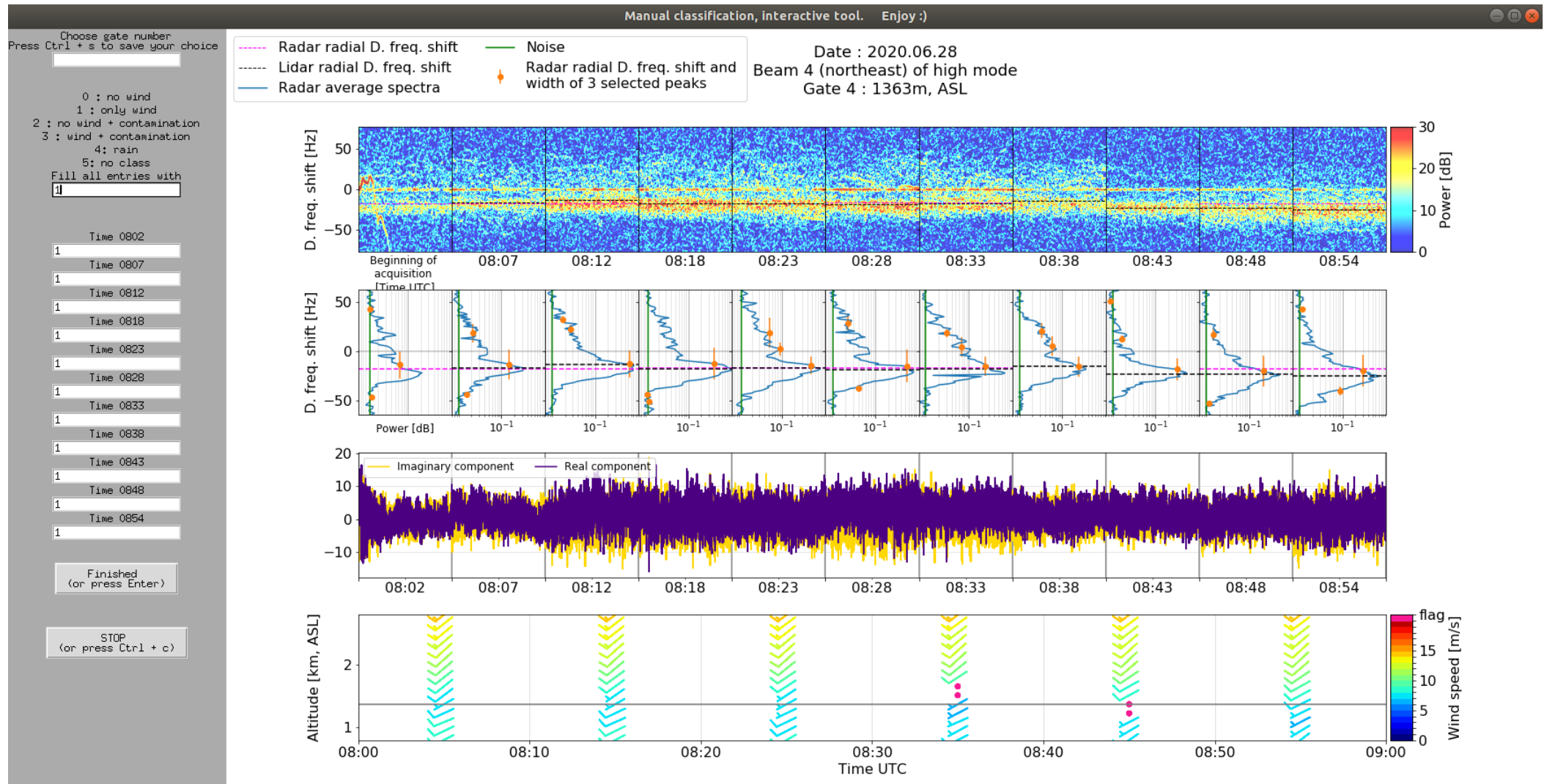


Figure 3.1: Manual classification graphical interface

For the remainder of the project, spectrograms presenting obvious signs of unique meteorological conditions as rain, drizzle or clouds are discarded (see Figures A.1, A.2 and A.3 in Appendix A). The time serie is used as a guideline to identify contamination. Moreover, based on findings from section 2.3, beams 4 and 5 are considered in the first place as they show greater correlations. The overall objective is to get samples belonging to one and only one well-defined class with coherent lidar Doppler frequency shift.

After several days of work, the following dataset is established. The validation set is randomly selected from the train set. The test set is arranged for days July 11 and 12, 2020. The reason for this choice lies in the representativeness of a 2-month dataset along with the condition of non-correlation among sets and samples. It is not possible to pick the very end of the period as validation and test sets as it mostly rained over those days. The method applied allows a check on both random mix and temporal split influence while having made a deliberate choice regarding the test days.

**Table 3.1:** Classification dataset

Class	Definition	Total	Train	Validation	Test
		# of samples	[class-wise %]	[class-wise %]	[class-wise %]
0	No wind	2103	80.7	10.2	9.10
1	Only wind	2095	78.8	9.60	11.6
2	Contamination	2119	78.0	9.60	12.4
3	Cont. + wind	1383	72.2	13.0	14.8
			[total-wise %]	[total-wise %]	[total-wise %]
		7700	<b>77.9</b>	<b>10.4</b>	<b>11.7</b>

### 3.1.2 Spectrogram and additional features preprocessing

The output of the discrete Gabor transform is subject to a log transform, its units henceforth becoming debibels. The scale is variable, ranging from  $-10^2$  to  $10^2$  at most. Scarse negative values are assigned to 0 as spectrograms are mainly positive. If greater than 30, values are brought back to 30. It has proven relevant to preserve the range from one spectrogram to another. A vertical gradient to detect horizontal features (wind) was also tested but without success.

A rotation of  $180^\circ$  is applied to the spectrograms of class 3, which was under-represented with originally half the samples presented in [Table 3.1](#).

Noise and time serie maximum, that is the maximum absolute value of either the imaginary or the real part of the signal, are additional features. Both are normalised using their respective minimum and maximum on the train set. [Figure 3.2](#) shows their histograms stacked per class for all 3 sets. The noise level is lower for class 0 than for class 2. Moreover, the time serie maximum covers specific ranges for each class.

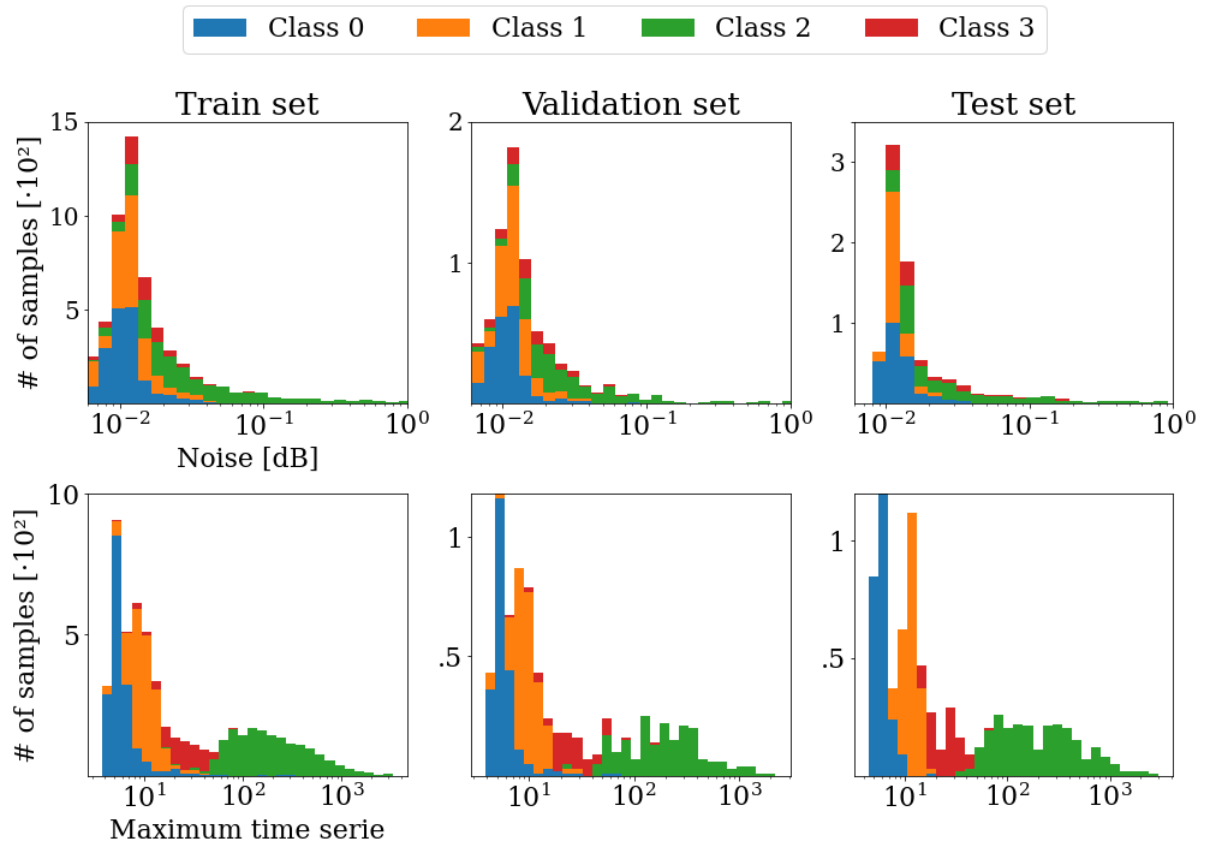


**Figure 3.2: Additional features distributions**

Noise (1<sup>st</sup> row) and time serie maximum (2<sup>nd</sup> row) for all 3 sets (columns)

### 3.1.3 Classification model

The numbers 600 and 544 refer to frequency (axis 0, y-axis) and acquisition time (axis 1, x-axis) respectively. A batch normalisation on axis 1 is carried out first. Thereafter, one

convolution with activation ReLU brings the third dimension to 16. The convolution kernel spans on the whole frequency axis (see [Figure B.13](#)).

An average pooling layer divides the first dimension by 2 and reduces the second to 1 as it extends on a height of 544. It decreases the flatten layer lenght and allows to maintain a resonable network size compared to the number of samples available (a few hundred thousands trainable parameters, see [Figure B.14](#)).

A neural network comprised of one dense layer of 32 neurons comes consecutively. Its output is concatenated with the additional features aforementioned. A last dense layer with softmax activation outputs the prediction to belong to each of the 4 classes.

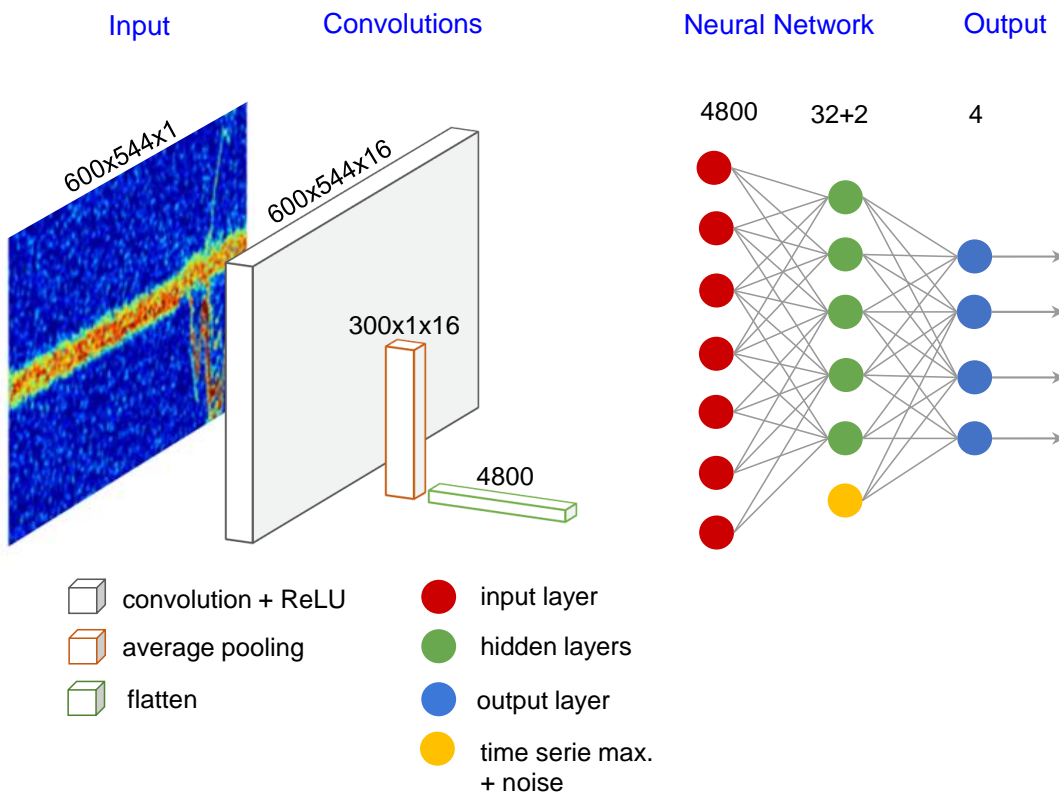


**Figure 3.3: Classification model.** See Figures [B.13](#) and [B.14](#) for more details

Adam optimizer is chosen, without any learning rate. As dropout layers, it leads to a validation performance always higher than the one of the training set.

### 3.1.4 Loss and metrics

The actual/true classes are encoded as one-hot labels, as shown in 3.1. The prediction is a probability to belong to each of the 4 classes. The highest probability defines the predicted class.

$$\text{class 0} = \begin{bmatrix} 1 \\ 0 \\ 0 \\ 0 \end{bmatrix} \quad \text{class 1} = \begin{bmatrix} 0 \\ 1 \\ 0 \\ 0 \end{bmatrix} \quad \text{class 2} = \begin{bmatrix} 0 \\ 0 \\ 1 \\ 0 \end{bmatrix} \quad \text{class 3} = \begin{bmatrix} 0 \\ 0 \\ 0 \\ 1 \end{bmatrix} \quad (3.1)$$

The loss is a categorical cross-entropy. Cross-entropy is a measure of the difference between two probability distributions for a given random variable or set of events.

$$\text{categorical cross-entropy} = - \sum_{n=1}^N y_{true}^n \cdot \log y_{predicted}^n \quad (3.2)$$

with  $y_{true}$  and  $y_{predicted}$  the actual and predicted values (no units) and  $N$  the set total number of samples.

Additional metrics are implemented:

$$\text{accuracy} = \frac{TP + TN}{TP + TN + FP + FN} \quad (3.3)$$

$$\text{precision} = \frac{TP}{TP + FP} \quad \text{recall} = \frac{TP}{TP + FN} \quad (3.4)$$

with TP the true positives, TN the true negatives, FP the false positives and FN the false negatives.

## 3.2 Regression

### 3.2.1 Manual selection of coherent dataset

When manually classifying the dataset, samples with visually coherent lidar Doppler frequency shifts only are withheld. All spectrograms are rotated by 180°. Some of them

did not have associated lidar value which explains the differences in numbers between [Table 3.1](#) and [Table 3.2](#).

As before, the validation set is obtained with a random split. The test set is constituted of days June 28, July 10, 11 and 14, 2020. They are chosen in order to get well distributed frequencies covering most of the range enclosed in the train and validation sets.

**Table 3.2:** Regression dataset

Class	Definition	Total	Train	Validation	Test
		# of samples	[class-wise %]	[class-wise %]	[class-wise %]
1	Only wind	2296	79.4	9.1	11.5
3	Cont. + wind	1004	82.2	9.2	8.6
			[total-wise %]	[total-wise %]	[total-wise %]
		3300	<b>80.3</b>	<b>9.1</b>	<b>10.6</b>

### 3.2.2 Spectrogram and additional features preprocessing

Spectrograms are pre-processed as described in [subsection 3.1.2](#). When flipped, the associated Doppler frequency shifts are multiplied by -1.

They have different frequency ranges (see [Figure 4.3](#)), it thus becomes essential to bring back the lidar Doppler frequency shift to the scale of the image as follows:

$$f_{norm} = \frac{f_r}{f_{rmax}} \quad (3.5)$$

with  $f_{norm}$  the normalised shift (no units),  $f_r$  the lidar radial Doppler frequency shift in Hz and  $f_{rmax}$  the maximum radial Doppler frequency shift of the spectrogram in Hz.

[Figure 3.4](#) presents  $f_r$  and  $f_r^{max}$  distributions on the 1<sup>th</sup> and 2<sup>nd</sup> rows. The last row is obtained with [Equation 3.5](#). Hence, the regression target is normalised and the scale of the image respected.

The maximum frequency for each spectrogram is supplemented to the model as additional feature and is itself normalised using its minimum and maximum on the train set.

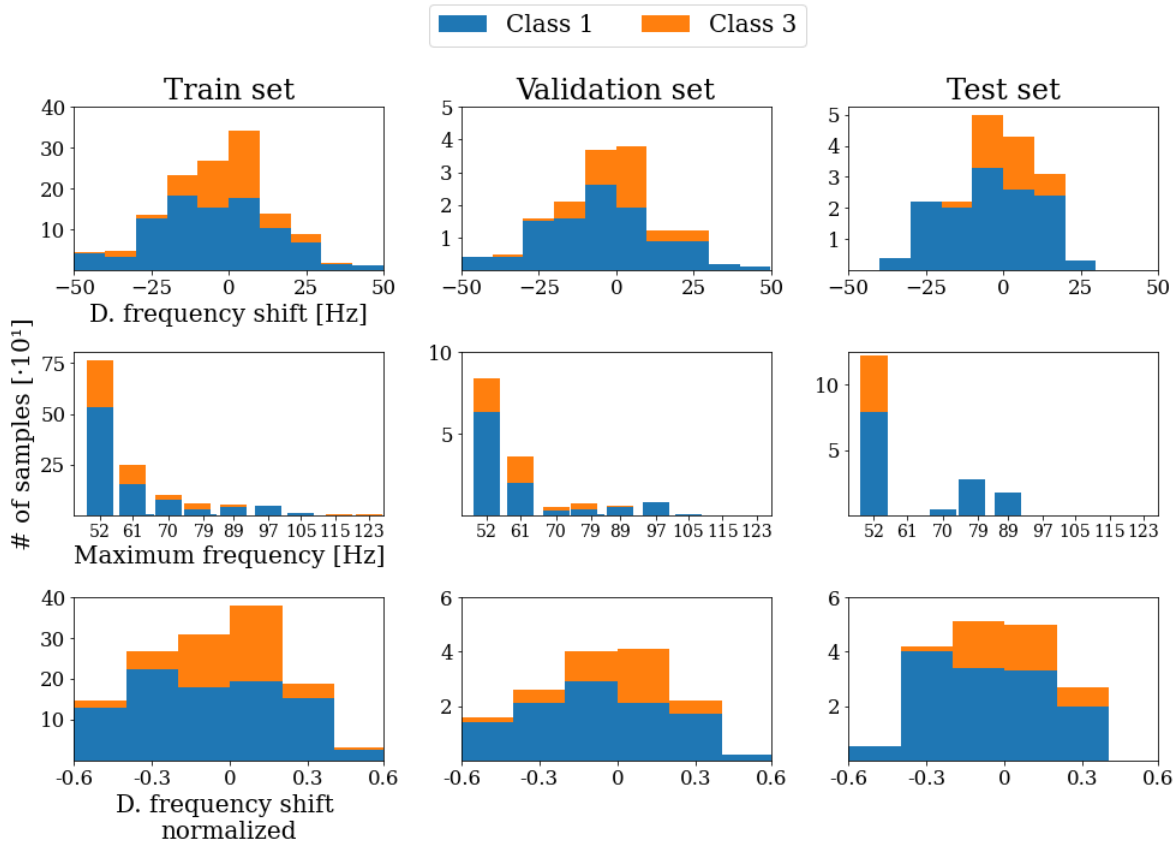


**Figure 3.4: Target and additional features distributions**

Lidar radial Doppler frequency shift (1<sup>th</sup> row), maximum radial Doppler frequency shift of the spectrogram (2<sup>nd</sup> row) and normalised Doppler frequency shift (3<sup>rd</sup> row) for all 3 sets (columns)

### 3.2.3 Regression model

Several layers of double convolution with ReLU activation are stacked together, bringing the third dimension to increase from 16 to 128. They are interspersed by average pooling layers which halve the first and second dimensions. The last average pooling kernel extends on the whole second dimension, allowing once again to bring the number of trainable parameters to a reasonable number.

A Neural Network follows with 2 dense layers, the additional feature being added to the last one. The output layer releases a normalised Doppler frequency shift prediction after a linear activation.

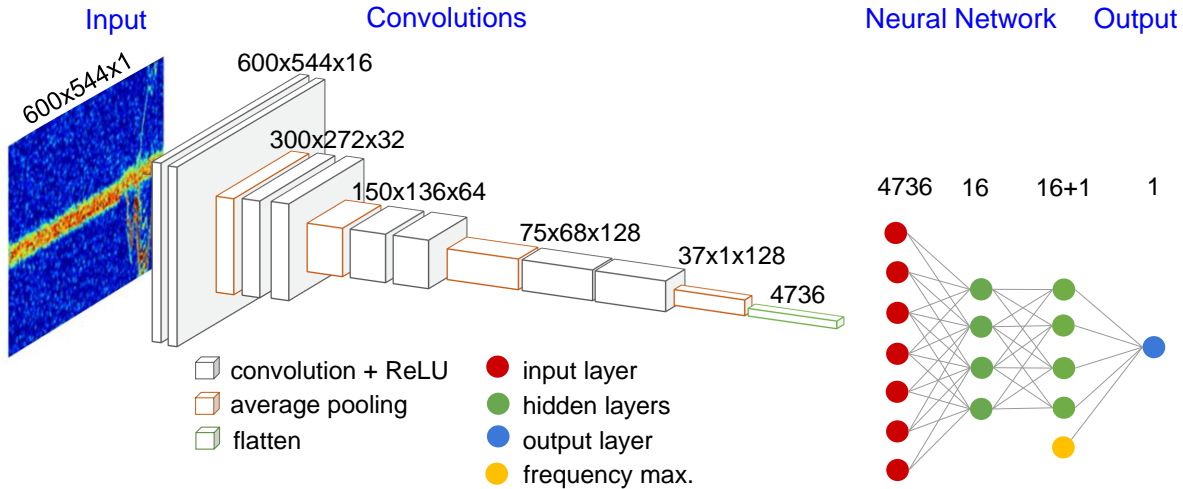


**Figure 3.5: Regression model.** See Figures B.15 and B.16 for more details

Adam optimizer is chosen, without any learning rate. As dropout layers, it leads again to a validation performance always higher than the one on the training set.

### 3.2.4 Loss and metrics

A Mean Squared Error (MSE) is chosen as the loss. It reduces the opportunity to predict outliers. Indeed, a MSE magnifies bigger errors which take a penalty of a square of their value, unlike a Mean Absolute Error (MAE).

A custom weighted metric is implemented in TensorFlow, to be able to express the MAE with units  $\text{m s}^{-1}$ :

$$\text{MAE}_{\text{weighted}} = \sum_{n=1}^N f_{rmax}^n \cdot |y_{true}^n - y_{predicted}^n| \quad (3.6)$$

with  $f_{rmax}$  the maximum radial Doppler frequency shift of the spectrogram in Hz,  $y_{true}$  and  $y_{predicted}$  the actual and predicted values (normalised, no units) and  $N$  the set total number of samples.

# 4 Results and discussion

Results obtained for the classification and the regression are presented in this chapter. The reader is then provided with suggestions and ideas for future research.

The selected checkpoints for both models are saved and the TFRecord test files are available. Tests can be run and will produce the reported results. It would involve downloading the repository, installing the Python requirements, running the specific codes and a GPU. The GPU is required because of certain implementations that are not supported by a CPU (batch normalisation layer on axis 1 for example).

## 4.1 Classification

After a certain number of epochs, train and validation losses start diverging which means the model overfits. Epoch 58 is selected as it shows the lowest validation loss and the maximum validation accuracy and precision.

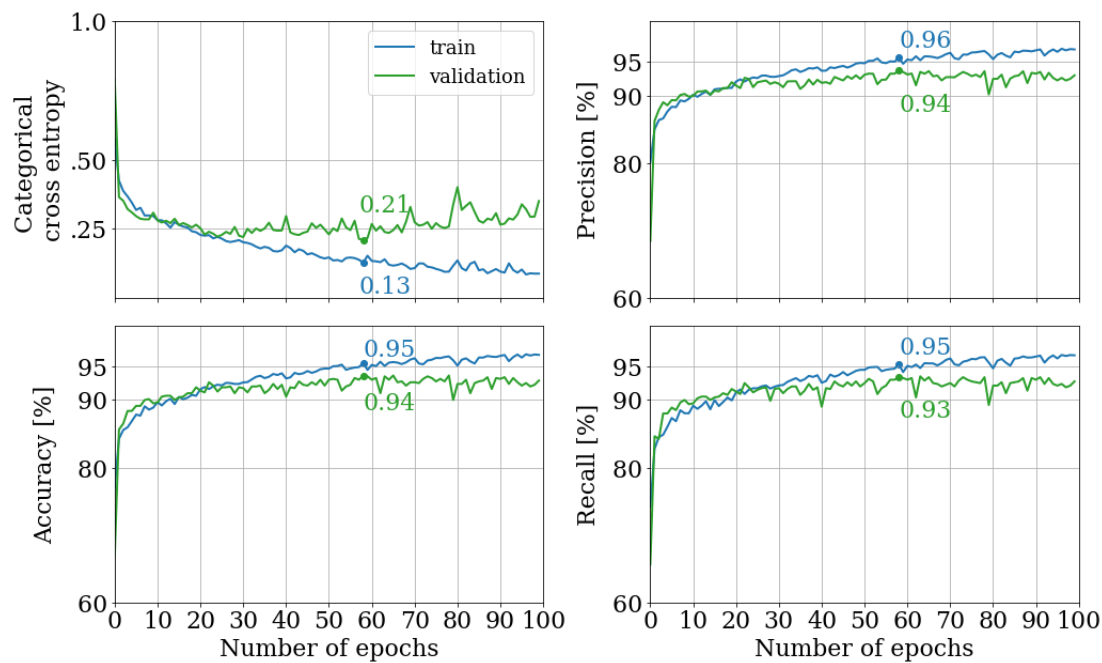


**Figure 4.1: Classification training loss and metrics.** Epoch 58 is selected

The test set obtains a loss of 0.19, slightly lower than the validation loss. Test accuracy, precision and recall are of 94%. The confusion matrix of [Table 4.1](#) shows the origine of the inaccuracy and imprecision: classes 1 and 3 are sometimes confounded as well as classes 2 and 3.

**Table 4.1:** Confusion matrix on the test set

True Predicted \	0	1	2	3
No wind	239	1	0	0
Only wind	1	201	0	15
Contamination	0	0	248	16
Cont. + wind	0	7	17	158

A few examples of well and mis-classified spectrograms are shown in Figures [4.2](#) and [4.3](#). All spectrograms in train, validation and test sets are available [here](#).

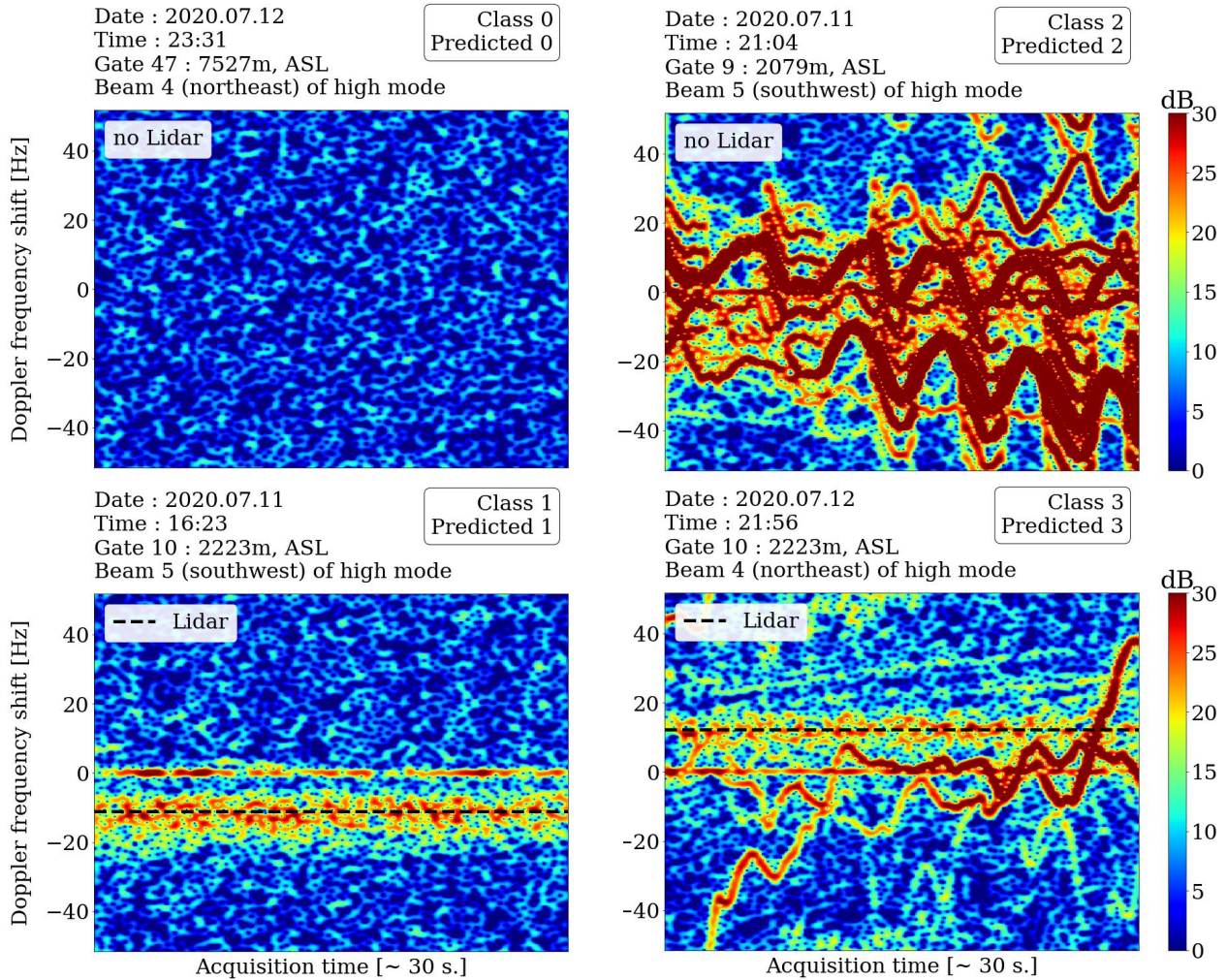


**Figure 4.2: Well classified spectrograms (test set).**

All well classified samples of the test set are available [here](#)

Class 0 spectrograms (upper left, [Figure 4.2](#)) have no wind measured by the instrument. Class 1 (lower left) presents a symmetrical line at 0 frequency which is due to the ground clutter. However the latter is not considered as contamination in the framework of the present thesis. Besides, the model seems to differentiate the ground clutter from the wind signal. The latter can be clearly perceived. The lidar Doppler frequency shift is visually coherent. Class 2 (upper right) displays heavy contamination and the wind can not be distinguished at all. Eventually, the spectrogram classified as 3 (lower right) shows a rather substantial contamination which does not cover the wind signal. All 4 are well classified by the algorithm.

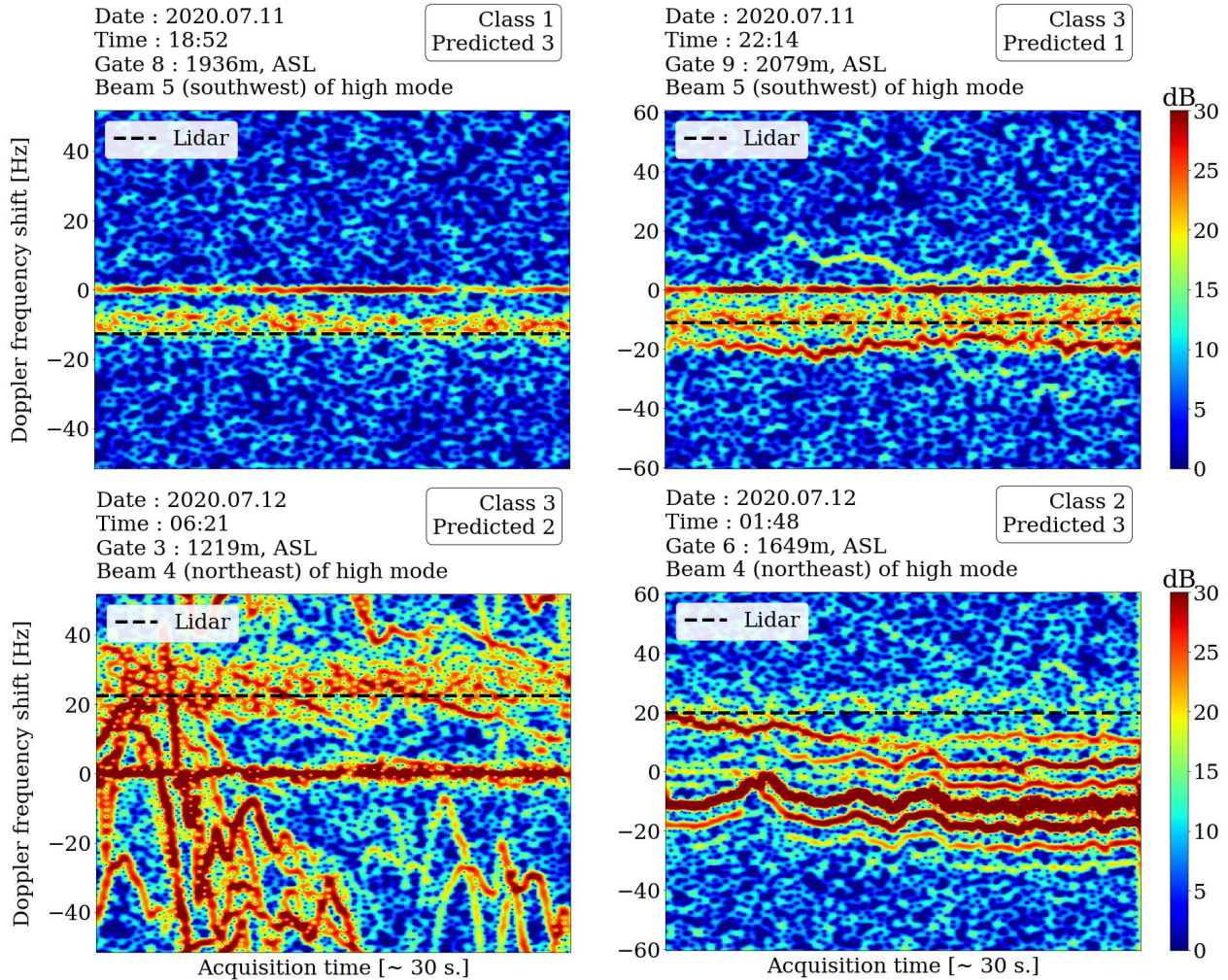


**Figure 4.3: Misclassified spectrograms (test set).**

All misclassified samples of the test set are available [here](#)

Note the different frequency ranges mentioned in [subsection 3.2.2](#)

Classes 1 and 3 can be hard to perceive as shown in [Figure 4.3](#). The spectrogram in the upper left corner does not show a significant difference to [Figure 4.2](#) lower left (class 1), besides the fact that the wind signal is slightly more condensed. The spectrograms on the right hand side show bird contamination appearing horizontally which might have been misleading the model. Eventually, class 3 misclassification into 2 can be due to heavy contamination intersecting the wind signal (lower left).

## 4.2 Regression

As before, epoch 46 is held before the model starts overfitting with a train MAE of  $0.21 \text{ m s}^{-1}$  and a validation MAE of  $0.24 \text{ m s}^{-1}$ .

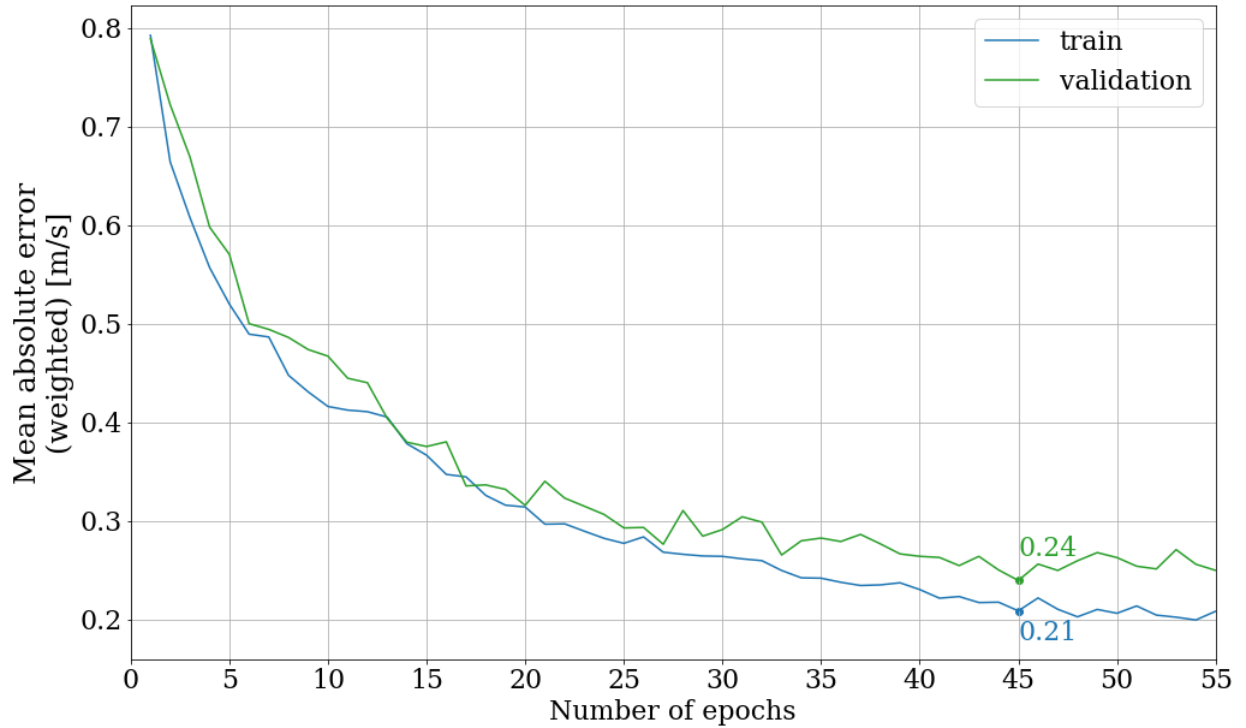


**Figure 4.4: Regression custom MAE**  
Epoch 46 is selected

The test set achieves a MAE of  $0.22 \text{ m s}^{-1}$  ( $1.87 \text{ Hz}$ ) with an  $R^2$  of 0.97 (see [Figure 4.5](#)). All spectrograms in train, validation and test sets are available [here](#).

Larger errors come from larger shifts, most probably because they are underrepresented in the dataset. Class 1 (only wind) and 3 (wind and contamination) present the same error orders of magnitude on velocity shifts lying between  $-2$  and  $2 \text{ m s}^{-1}$ , that is 0.176 and 0.170 respectively. On the whole range, class 1 MAE is of  $0.232 \text{ m s}^{-1}$  and class 3 of 0.171 due to the bias notable on the negative tail. Spectrograms with actual Doppler shift and predicted values are shown in [Figure 4.4](#).

The question of two separate models, one for class 1 and another one for class 3 has been raised. It proves to be unnecessary as the errors for both classes are comparable when using only one model.

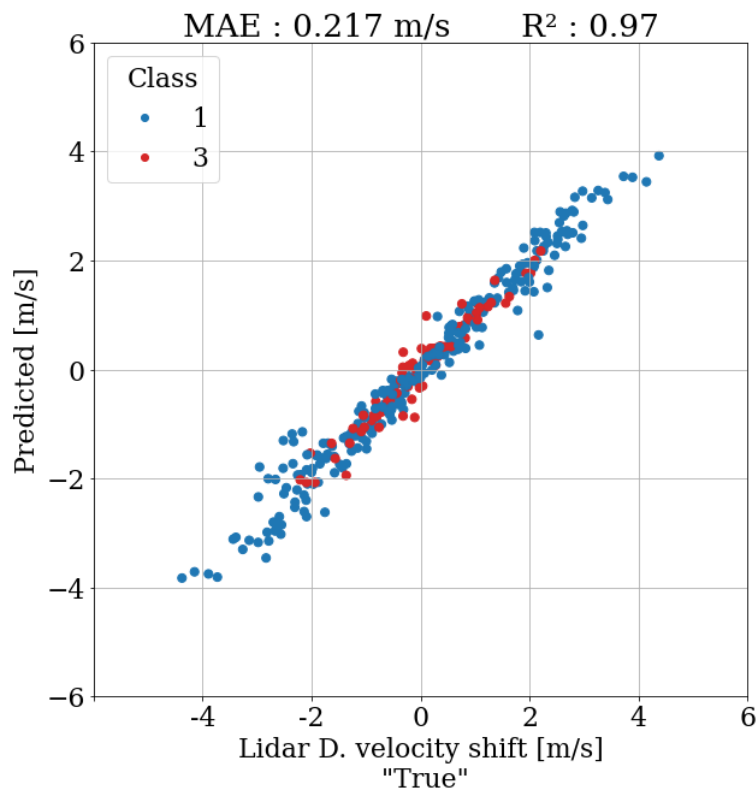


**Figure 4.5: Scatter plot on the test set with the representation of the two classes**

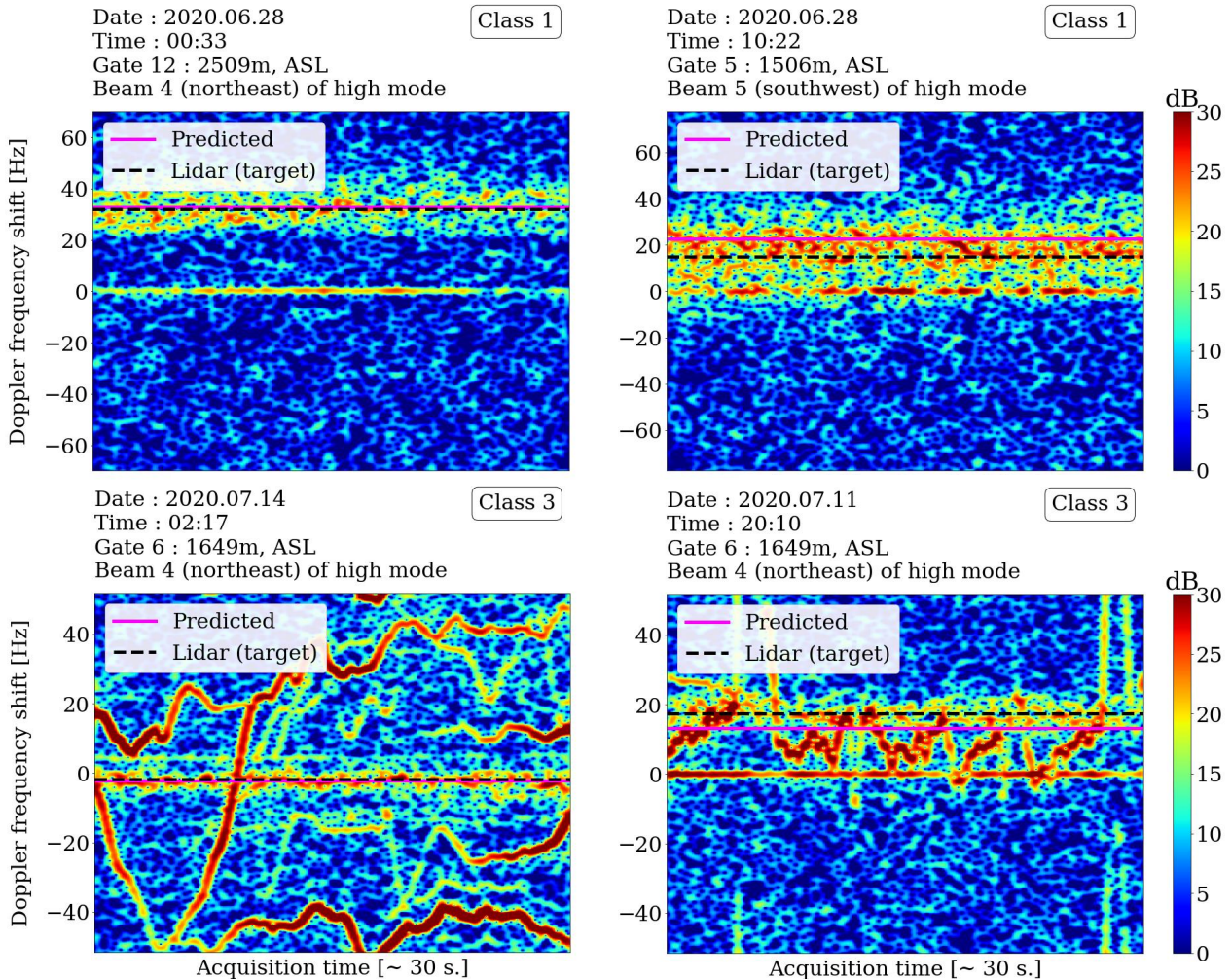


**Figure 4.6: Example of predicted and actual/true/lidar Doppler velocity shifts on spectrograms.**

All test set samples are available [here](#)

The left-hand column of Figure 4.6 shows intriguingly good outcomes for class 1 and for class 3, presenting rather abundant contamination. The right-hand column reveals examples where the model is not as competitive. For class 1, it is probably inherent to the broad spread of the wind signal. Class 3 is a difficult sample where contamination significantly covers the wind frequency.

## 4.3 Discussion

### 4.3.1 Model generalisation

As mentioned, spectrograms have been manually classified with the aim of ensuring samples belonging to one and only one well-defined, and therefore restrictive, class. It is not illustrative for the entire dataset which would require the use of many more classes. In particular, not all meteorological conditions are duly represented. The issue then becomes the lack of clear boundaries between classes.

Times 02:22 or 02:46 of [Figure 2.3](#) and additional Figures [A.10](#) and [A.11](#) illustrate the doubts raised when manually classifying. Is the wind still visible enough ? Does the lidar Doppler shift help to determine whether we see it or not ? Can the model detect it even if it is not visible for the human eye ? But even more importantly: Do the neighbouring spectrograms influence the choice on this particular case ? Is the contamination too light to consider the spectrogram as contaminated ?

The concept of classes that are not mutually exclusive might help solving some of those questions. Yet, one will have to make sure to stay consistent while going through the manual classification task. It can be done via the choice of objective criteria such as the time serie maximum for example.

With the idea of a functional implementation, the model must be also be generalised to cover the entire period of the year and different sites, contamination or not. One solution may be to use different models depending on the season or area, if needed.

### 4.3.2 Dataset size

The split of the sets remains an open question. A dataset covering a longer period will allow a standard temporal split. Nevertheless, a larger dataset implies a sizable and time-consuming manual classification.

Classification might not ultimately necessary to achieve a functional implementation. If wrongly detected on too heavily contaminated spectrograms, the radial Doppler shifts involved will be flagged by subsequent filtering and quality control algorithms. The latter can be inspired by those already existing, naturally, while being readjusted to the method.

At a larger scale and without manually selecting visually concordant lidar shifts, one will need to ensure of the initial error supplied to the model. Correcting for resolution volumes

might be a chance to obtain better correlations between the two instruments. However, both do not measure the same object and react differently to specific meteorological conditions as rain, for example.

Several proposals can be made concerning this last point. Not using the lidar but manually determining the position of the wind would be one that is also ultimately time-consuming. Segmentation is also in line with this idea, implying different methods and models. In the end, the feature of interest is the wind and it can be captured in a rectangular bounding box. Eventually, spectrograms could be concatenated over 30 minutes to 1 hour. The regression target will then be an average, known as more stable and consistent. A sliding window moving from dwell to dwell might be considered.

### 4.3.3 Input data

As pointed out by [Lehmann et al. \(2008\)](#), it is beneficial to treat contamination before computing the transform. Up to now, no filtering of any kind is carried out in this project. It might be worth performing a Gabor filter on the spectrograms used as inputs and evaluating its impact on the wind velocity retrieval performance of the present method.

Another suggestion is to apply Machine Learning techniques in order to filter contamination from the time serie itself. It would ease the task in case of heavily contaminated dwells, which represented a significant number in this particular dataset.

Building future work on both former research, based on physical principles and statistical distribution tests, and modern methods can only be beneficial. Personally, I am of the opinion that both are absolutely complementary and I would not advise to rely on computing power only.

### 4.3.4 Real time implementation

By now, the task has proven possible, an effective model architecture is proposed and the input pipeline is developed. The latter deserves a review effectiveness-wise if scaling up the implementation. Further quality control steps adapted to the method will also be required.

Additionally, Python would need to be introduced as a tool on the Meteoswiss servers which is not the case yet. The processing of new measurements over all altitudes for the 5 beams will involve significant computational resources. A comparison with the

current demand might be necessary before going any further. A solid computing power availability will also be required if models are chosen to be trained continuously with new data.

# **Conclusion**

The existing processing methods and the current state of research has been assessed. With the initial motivation of further investigating bird contamination, the work opens up new processing prospects. The latter might improve the robustness of the method and the output product quality.

An evaluation of Doppler radar and lidar measurements correlations has been performed, with the objective of their simultaneous use in a new processing algorithm. It is the first innovative nature of this work. Both instruments tend to provide complementary advantages and can supplement each other.

Deep learning models are powerful tools which start to be too commonly employed for any kind of purpose. Whilst keeping in mind the importance of relating them to physical principles, one needs to master the basics of their use. Within the present framework, Convolutional Neural Networks revealed being particularly competitive.

This preliminary work covers a limited range of the many existing possibilities and thus only reveals the tip of the iceberg. A set of suggestions has been given for potential future research, with the aim of once achieving a 3D wind field reconstruction

# Appendix A

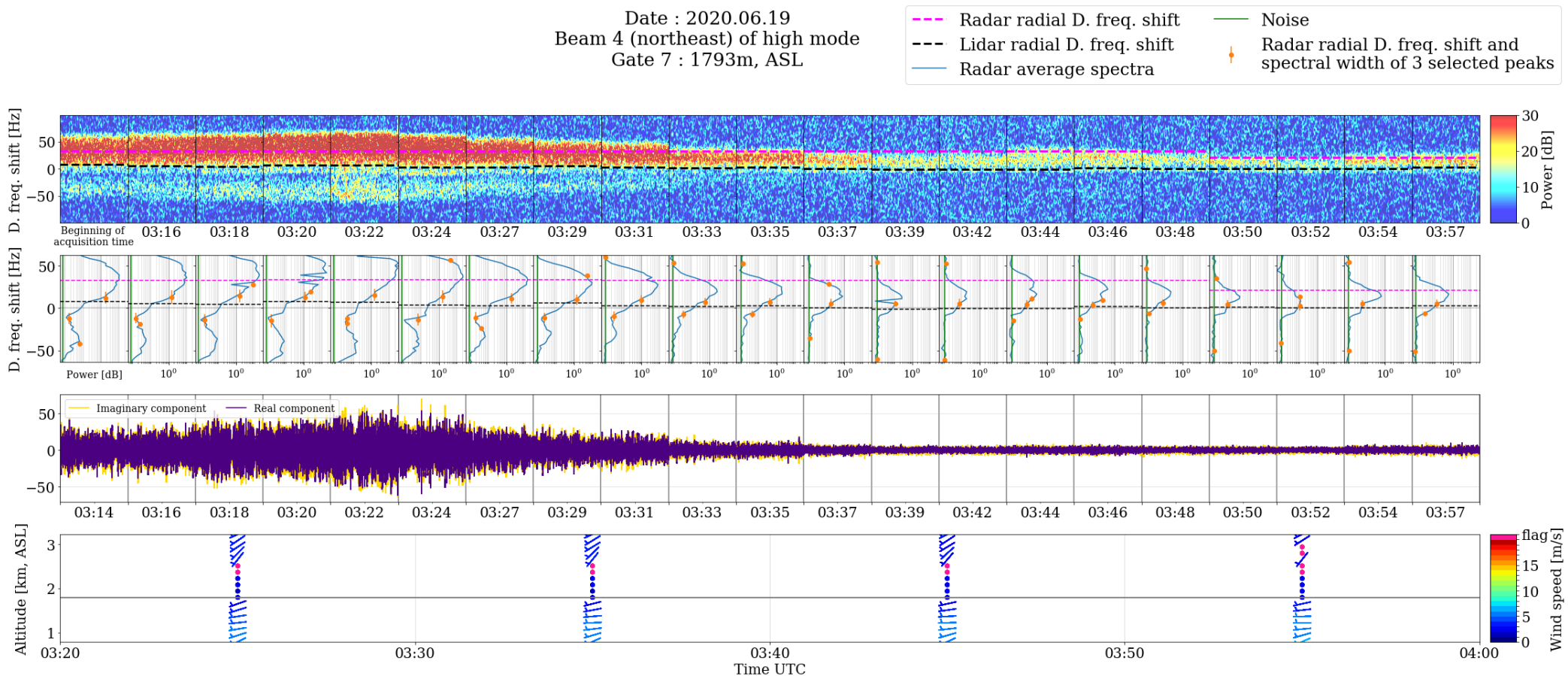


**Figure A.1: Precipitation event, confirmed by ground-based measurements at 03:10, 03:20 and 03:40 am UTC**

In such cases, the lidar tends to indicate a Doppler shift underlining the broadest and highest peak. The radar, in contrast, locates the average approximately on top of this peak. Please note that it is normal to not always have a radar average coinciding with one of the 3 selected peaks, especially if meteorological conditions or wind speed change abruptly. The second half an hour also shows inconsistencies between radar and lidar radial frequency shifts. The lidar value is visually incoherent.

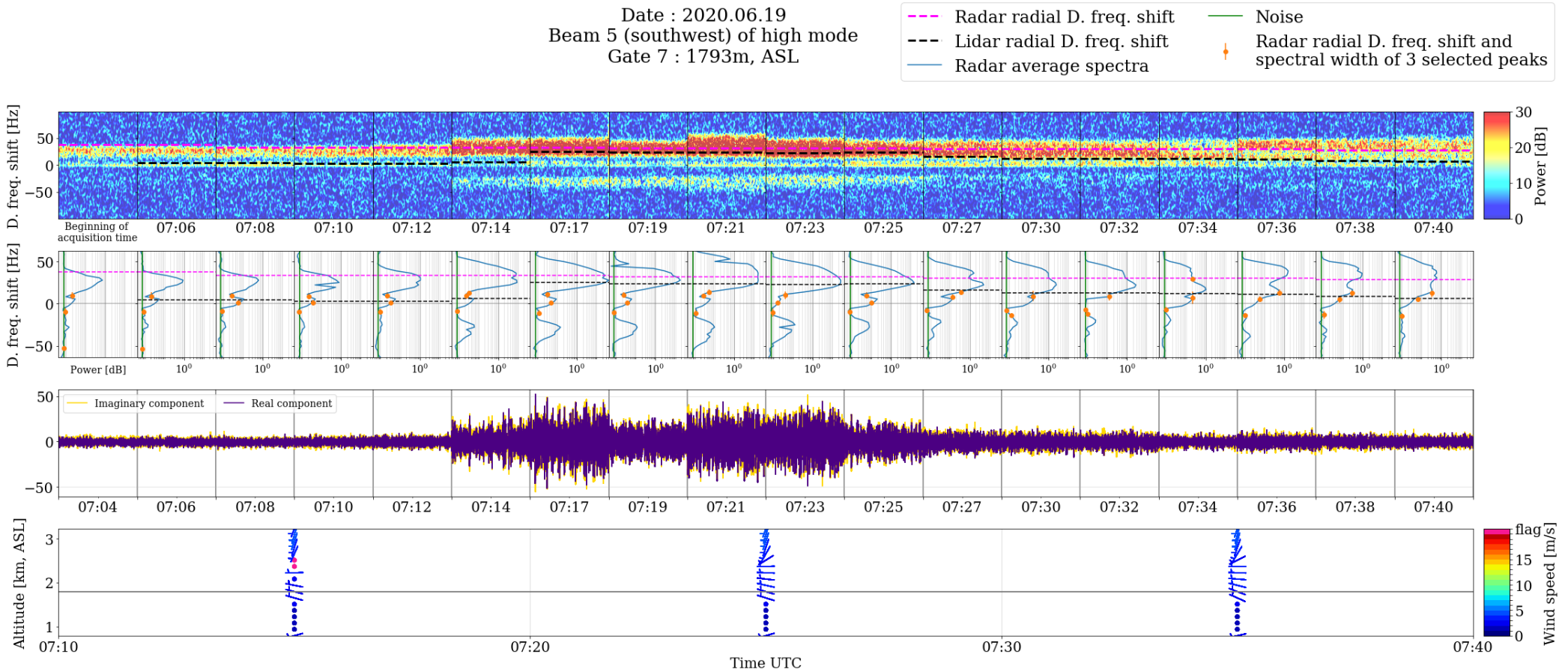


**Figure A.2: Precipitation event**

Ground-based measurements indicate rain at 6:00, 6:10, 6:30, 6:50 and from 7:50 to 08:10 am UTC i.e not within the period. The two distinct peaks mentioned Radenz et al. (2018) are visible on the average spectra at the beginning of the time serie. It is difficult to say where is the wind signal as the lidar shift moves all of a sudden at 7:17 am UTC. The third peak appearing at 7:14 am UTC in the negative frequency range seems to be an echo of the highest peak.

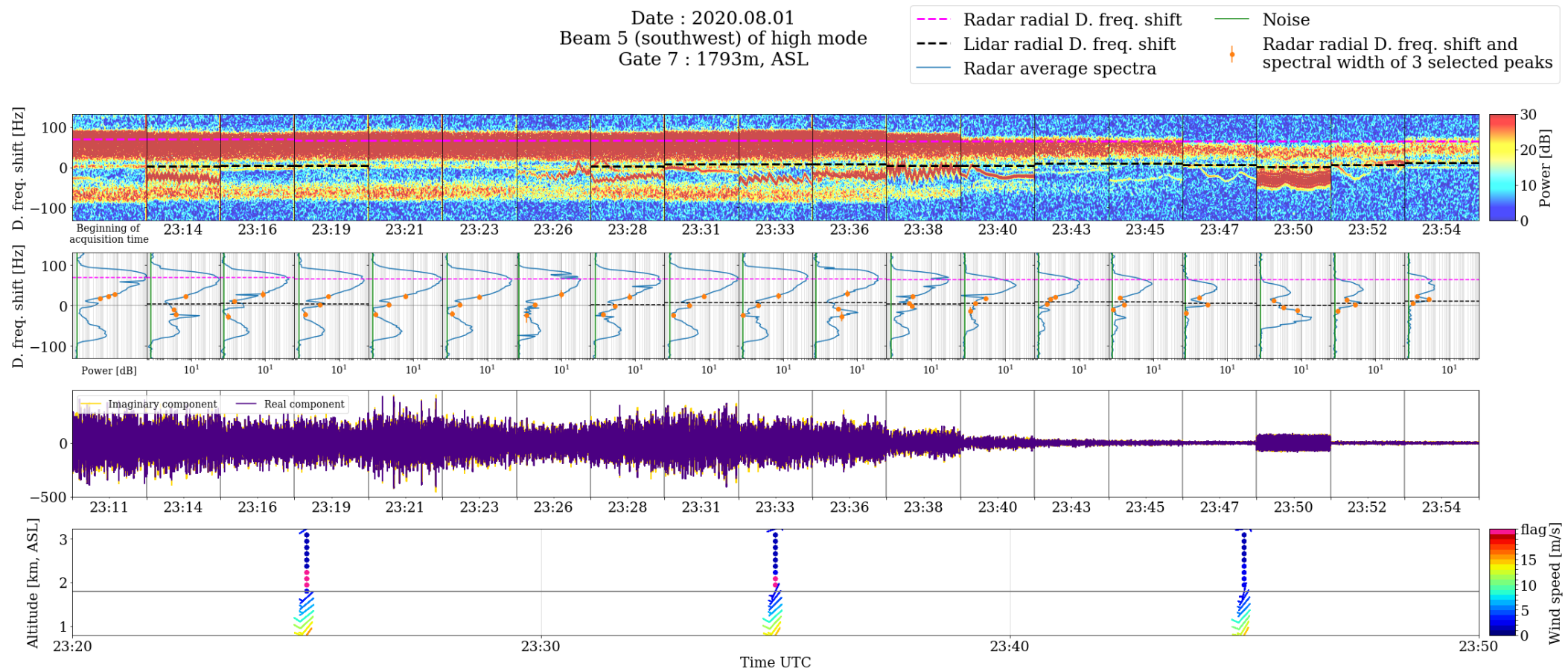


**Figure A.3: Rare case of bird contamination coupled with unfavourable meteorological conditions**

The lidar Doppler shift often overlaps with one of the selected peak. Once again the radar value is located higher as previous measurements influenced the average. The wind signal pointed out by the lidar is a bit more distinguishable than on the previous Figures A.1 and A.2 if zooming in.

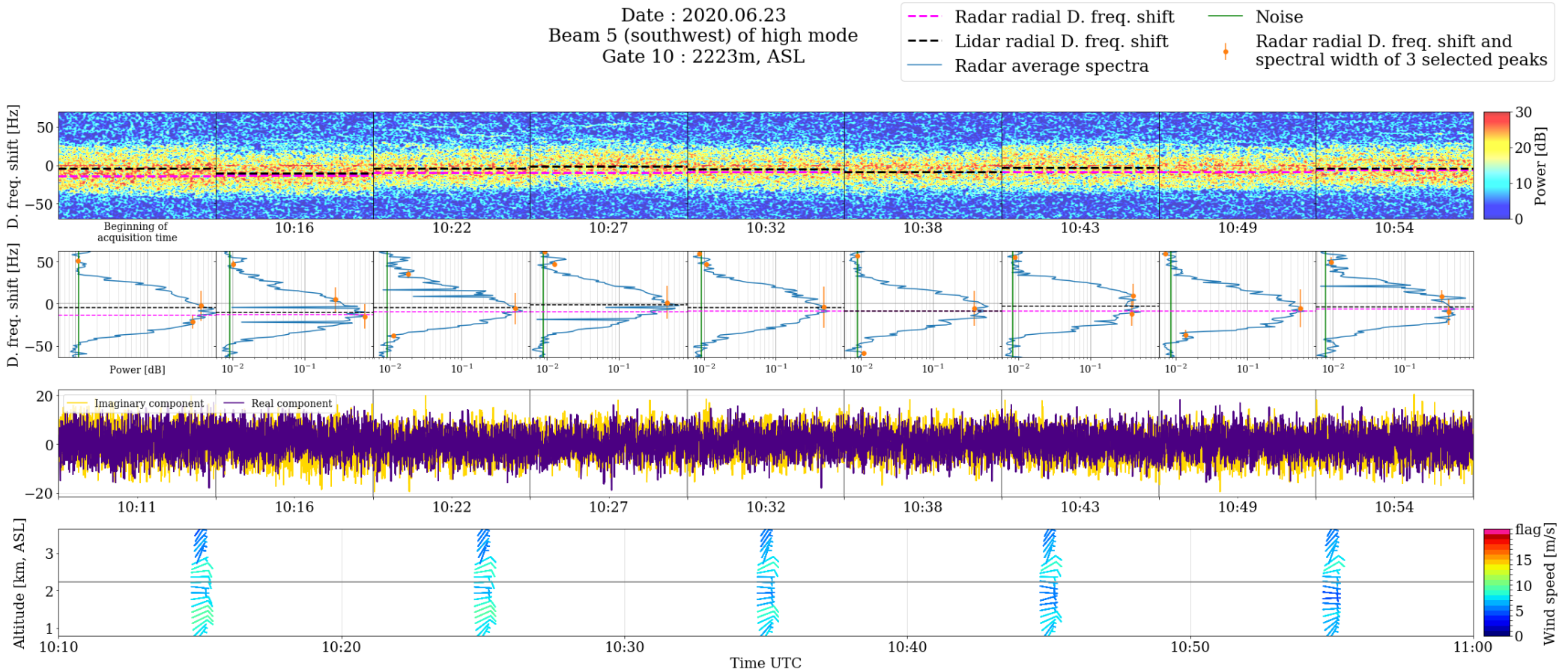


**Figure A.4: High spectral width, extended broad peak**

The top of the single predominant peak is undefined and incorporates smaller peaks. It is difficult to locate a Doppler frequency shift, and besides lidar and radar show small deviations.

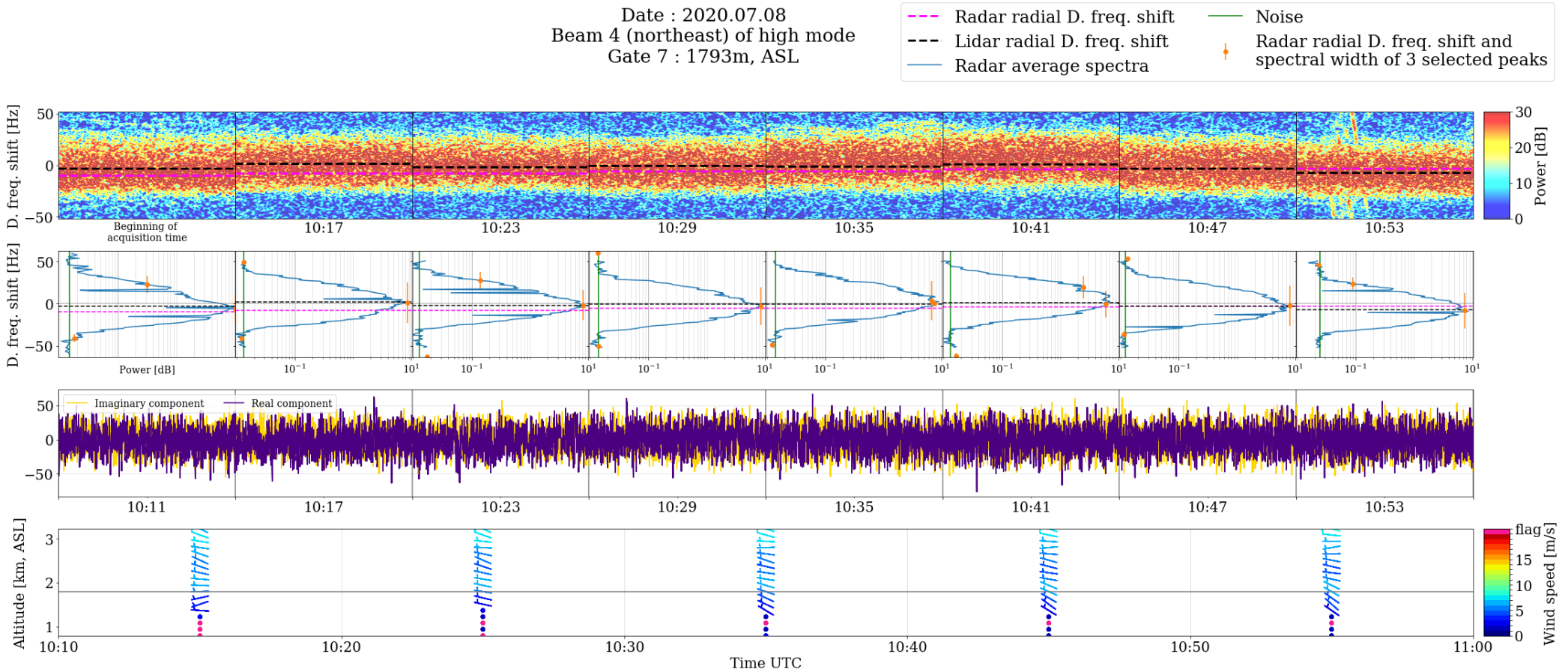


**Figure A.5: High spectral width, stronger signal**

The wind signal covers almost the entirety of the spectrogram. As for Figure A.4, the position of the Doppler frequency shift might be difficult to locate and could fluctuate.

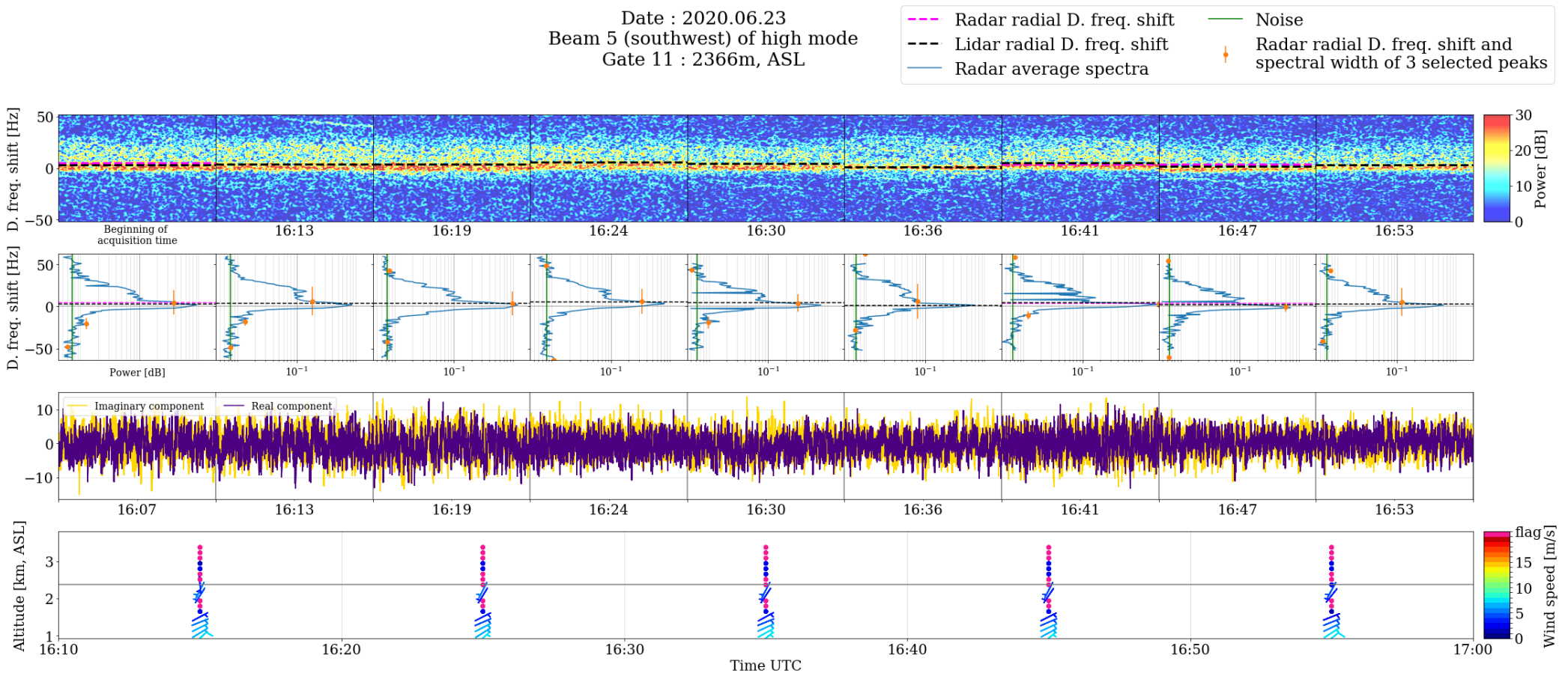


**Figure A.6: Ground clutter**

When the wind frequency shift approaches zero, it is sometimes complex to differentiate it from the ground clutter. The peak on the average spectra is utterly clear. However, the detected peak is most often shifted from the top of the curve. The highest point has probably been filtered (see [Figure 1.2, Filtering of peaks with special signatures](#)). On the spectrogram, it visually looks similar to ground clutter contamination (zoom in), yet the lidar indicates a Doppler shift close to zero.

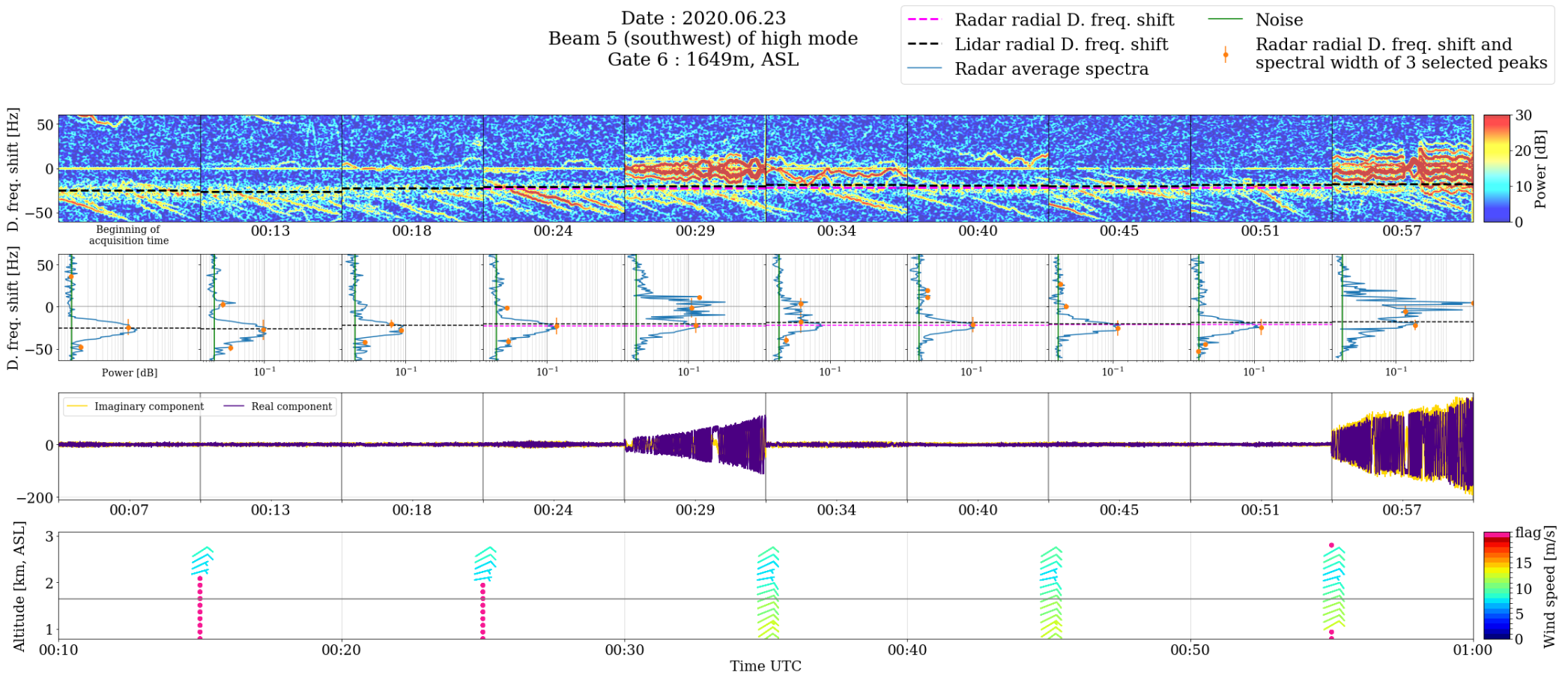


**Figure A.7: Illustration of the echo over several gates.** Compare with [Figure A.8](#) (144 m above).

According to Machine Learning principles, it would clearly not be appropriate for spectrograms of [Figure A.7](#) to end up in the train set if spectrograms of [Figure A.8](#) are in the test set, or vice versa.

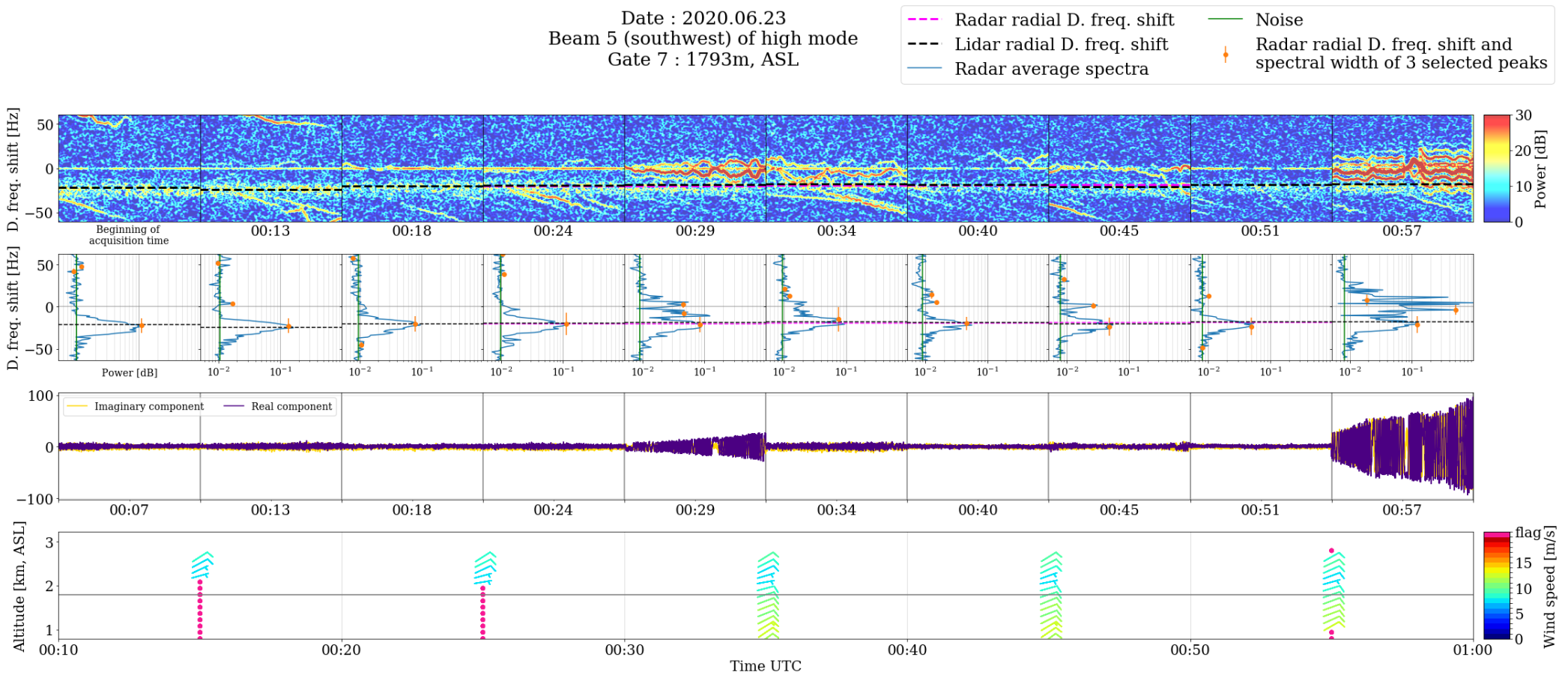


**Figure A.8: Illustration of the echo over several gates.** Compare with [Figure A.8](#) (144 m below).

According to Machine Learning principles, it would clearly not be appropriate for spectrograms of [Figure A.7](#) to end up in the train set when spectrograms of [Figure A.8](#) are in the test set, or vice versa.

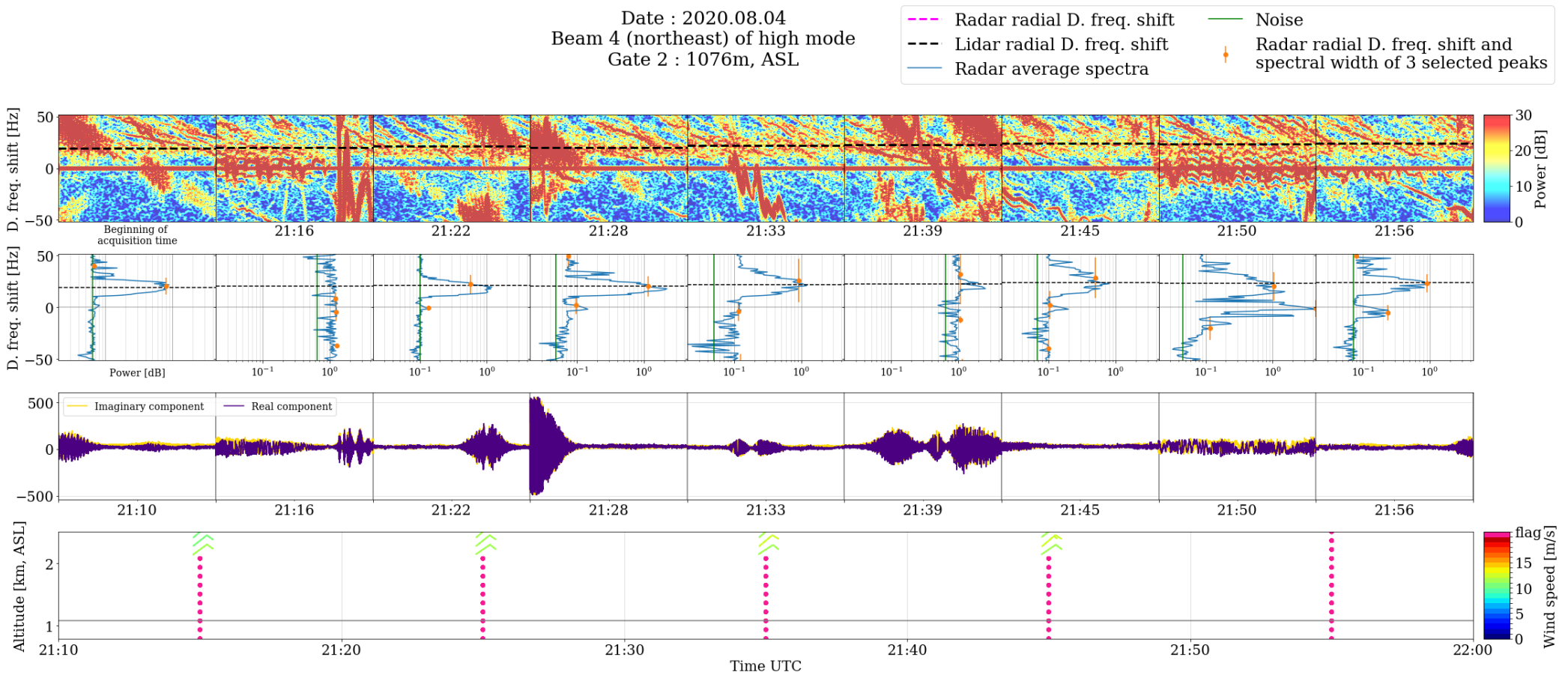


**Figure A.9: Specific contamination case.**

The wind signal is diagonally interrupted, making it harder to recognise its position as it shows several peaks.

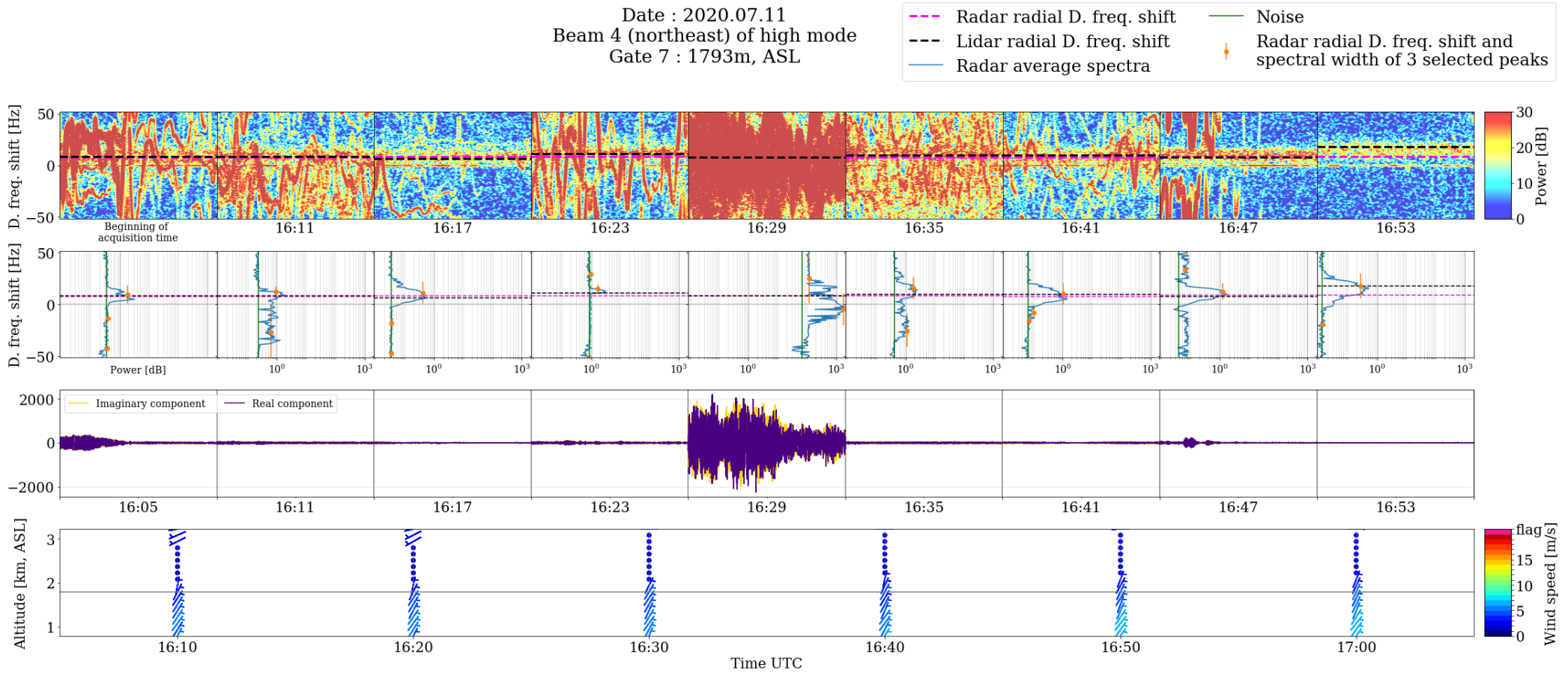


**Figure A.10: Heavy contamination example**

The wind might be still distinguishable by the model for times 04:05 pm (16:05), 04:11 pm (16:11) or 04:23 pm UTC (16:29). Such cases were discarded in the context of this preliminary work.

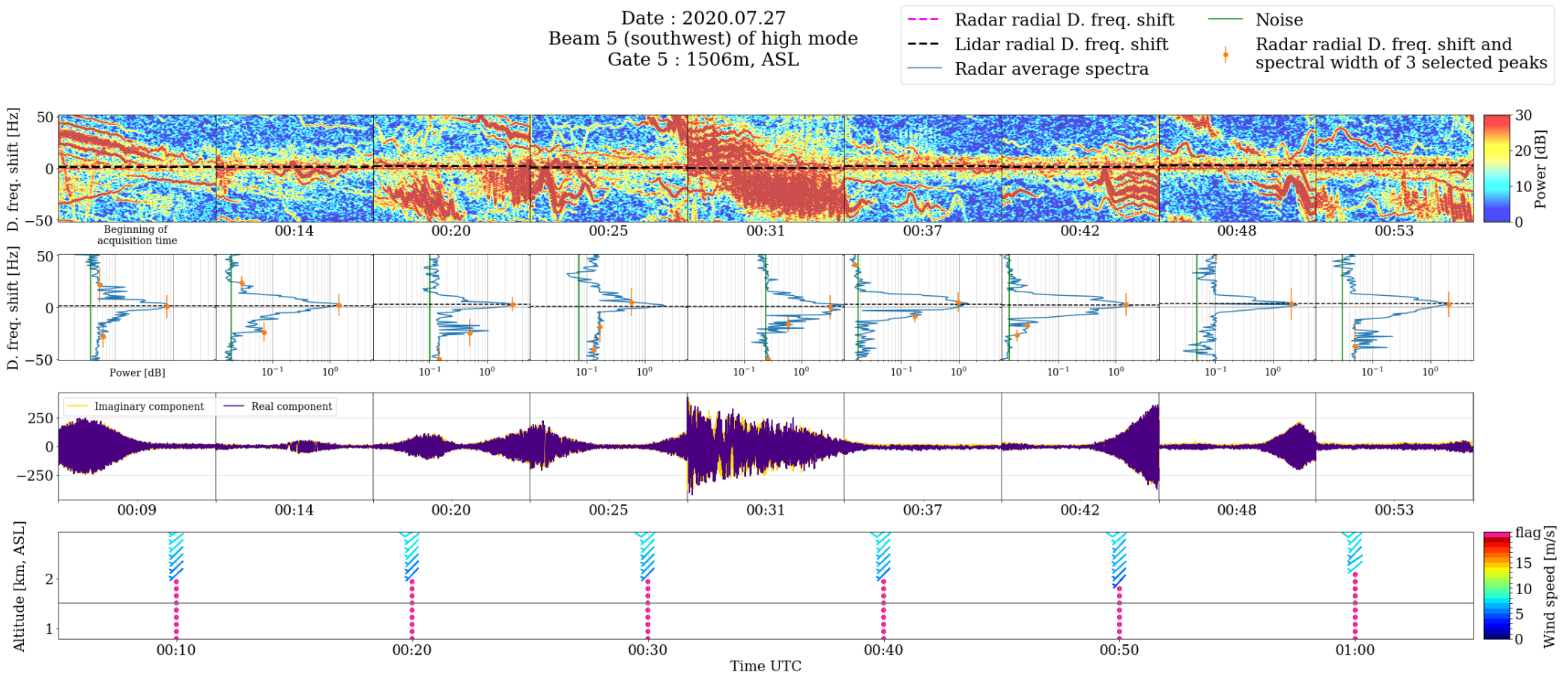


**Figure A.11: Heavy contamination and ground clutter**

Visually and relying on the lidar value, the wind frequency seems to be located just above the ground clutter. Yet, it could also be slightly under as can be seen at 00:53 am UTC for example. The wind signal is recognised by the model neither as wind nor as contamination. Such cases might be difficult to handle.

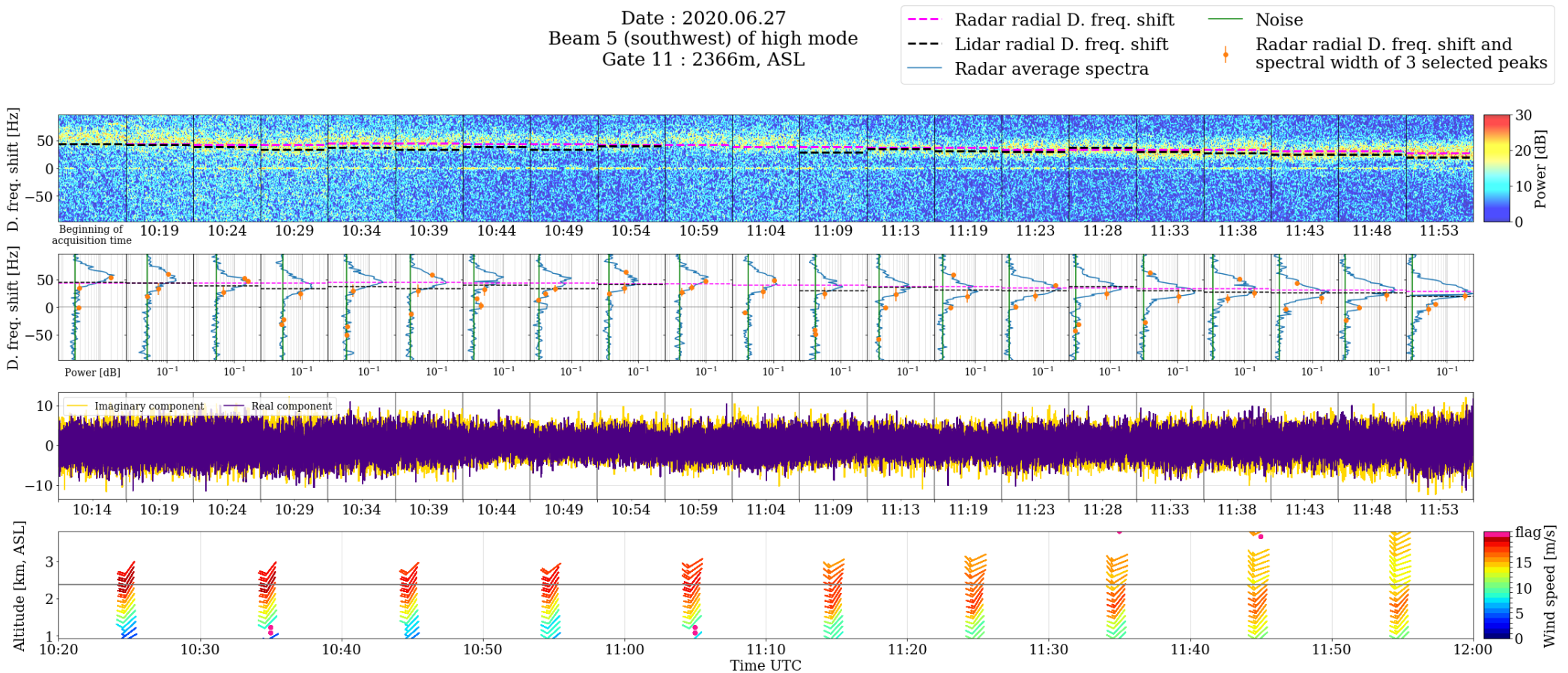


**Figure A.12: Clear wind signal example**

The lidar Doppler frequency shifts are most often visually coherent. Times 10:39, 10:49 or 11:09 am UTC were not held in the framework of this project because of the small discrepancies. However and surprisingly, the lidar value matches one of the selected peak.

# Appendix B

```
def ConvModel4(n_classes):

    y = Input(shape=(INPUT_HEIGHT,INPUT_WIDTH,1), name='Spectrogram', dtype='float32')
    y2 = Input(shape=(1,),name='Noise');
    y3 = Input(shape=(1,),name='TimeSerie');

    x = BatchNormalization(axis=1,name='Norm.Frequency')(y)

    x = Conv2D(16, (INPUT_HEIGHT, 3), padding="same",activation='relu',name='Layer1')(x)
    x = AveragePooling2D(pool_size=(2, x.shape[2]),name='Layer2')(x)

    x = Flatten(name='Layer3')(x)
    x = Dense(32, activation='relu',name='Layer4')(x)
    x = Concatenate(name='Layer5')([x,y2,y3])

    x = Dense(n_classes, activation='softmax',name='Ouput')(x)

    return Model(inputs=[y,y2,y3], outputs=x)
```

Figure B.13: Classification model. Python code

Layer (type)	Output Shape	Param #	Connected to
<hr/>			
Spectrogram (InputLayer)	[None, 600, 544, 1]	0	
Norm.Frequency (BatchNormalizat	(None, 600, 544, 1)	2400	Spectrogram[0][0]
Layer1 (Conv2D)	(None, 600, 544, 16)	28816	Norm.Frequency[0][0]
Layer2 (AveragePooling2D)	(None, 300, 1, 16)	0	Layer1[0][0]
Layer3 (Flatten)	(None, 4800)	0	Layer2[0][0]
Layer4 (Dense)	(None, 32)	153632	Layer3[0][0]
Noise (InputLayer)	[None, 1]	0	
TimeSerie (InputLayer)	[None, 1]	0	
Layer5 (Concatenate)	(None, 34)	0	Layer4[0][0] Noise[0][0] TimeSerie[0][0]
Ouput (Dense)	(None, 4)	140	Layer5[0][0]
<hr/>			
Total params: 184,988			
Trainable params: 183,788			
Non-trainable params: 1,200			

Figure B.14: Classification model  
TensorFlow output with dimensions

```

def ConvModel():

    input_shape=(INPUT_HEIGHT,INPUT_WIDTH,1)

    y = Input(shape=input_shape, name='Spectrogram', dtype='float32')
    y2 = Input(shape=(1,), name='FreqMaxNorm', dtype='float32')
    fweight = Input(shape=(1,), name='FreqMax', dtype='float32')

    x = Conv2D(16, (3, 3), padding="same",activation='relu',name='Layer1.1')(y)
    x = Conv2D(16, (3, 3), padding="same",activation='relu',name='Layer1.2')(x)
    x = AveragePooling2D(pool_size=(2, 2),name='Layer2')(x)
    x = Conv2D(32, (3, 3), padding="same",activation='relu',name='Layer3.1')(x)
    x = Conv2D(32, (3, 3), padding="same",activation='relu',name='Layer3.2')(x)
    x = AveragePooling2D(pool_size=(2, 2),name='Layer4')(x)
    x = Conv2D(64, (3, 3), padding="same",activation='relu',name='Layer5.1')(x)
    x = Conv2D(64, (3, 3), padding="same",activation='relu',name='Layer5.2')(x)
    x = AveragePooling2D(pool_size=(2, 2),name='Layer6')(x)
    x = Conv2D(128, (3, 3), padding="same",activation='relu',name='Layer7.1')(x)
    x = Conv2D(128, (3, 3), padding="same",activation='relu',name='Layer7.2')(x)
    x = AveragePooling2D(pool_size=(2, x.shape[2]),name='Layer8')(x)

    x = Flatten()(x)
    x = Dense(16,activation='relu',name='Layer9')(x)
    x = Dense(16,activation='relu',name='Layer10')(x)
    x = Concatenate(name='Layer11')([x,y2])
    x = Dense(1,activation='linear',name='Ouput')(x)

    return Model(inputs=[y,y2,fweight], outputs=x), fweight

```

**Figure B.15: Regression model.** Python code

Layer (type)	Output Shape	Param #	Connected to
Spectrogram (InputLayer)	[ (None, 600, 544, 1) 0		
Layer1.1 (Conv2D)	(None, 600, 544, 16) 160		Spectrogram[0][0]
Layer1.2 (Conv2D)	(None, 600, 544, 16) 2320		Layer1.1[0][0]
Layer2 (AveragePooling2D)	(None, 300, 272, 16) 0		Layer1.2[0][0]
Layer3.1 (Conv2D)	(None, 300, 272, 32) 4640		Layer2[0][0]
Layer3.2 (Conv2D)	(None, 300, 272, 32) 9248		Layer3.1[0][0]
Layer4 (AveragePooling2D)	(None, 150, 136, 32) 0		Layer3.2[0][0]
Layer5.1 (Conv2D)	(None, 150, 136, 64) 18496		Layer4[0][0]
Layer5.2 (Conv2D)	(None, 150, 136, 64) 36928		Layer5.1[0][0]
Layer6 (AveragePooling2D)	(None, 75, 68, 64) 0		Layer5.2[0][0]
Layer7.1 (Conv2D)	(None, 75, 68, 128) 73856		Layer6[0][0]
Layer7.2 (Conv2D)	(None, 75, 68, 128) 147584		Layer7.1[0][0]
Layer8 (AveragePooling2D)	(None, 37, 1, 128) 0		Layer7.2[0][0]
flatten (Flatten)	(None, 4736) 0		Layer8[0][0]
Layer9 (Dense)	(None, 16) 75792		flatten[0][0]
Layer10 (Dense)	(None, 16) 272		Layer9[0][0]
FreqMaxNorm (InputLayer)	[ (None, 1) ] 0		
Layer11 (Concatenate)	(None, 17) 0		Layer10[0][0] FreqMaxNorm[0][0]
FreqMax (InputLayer)	[ (None, 1) ] 0		
Ouput (Dense)	(None, 1) 18		Layer11[0][0]

Total params: 369,314  
Trainable params: 369,314  
Non-trainable params: 0

**Figure B.16: Regression model.** TensorFlow model with dimensions

# Bibliography

- Cohn, S., Brown, W., Martin, C., Susedik, M., Maclean, G., & Parsons, D. (2001a). Clear air boundary layer spaced antenna wind measurement with the Multiple Antenna Profiler MAPR.
- Cohn, S. & Goodrich, R. (2002). Radar wind profiler radial velocity: A comparison with Doppler lidar. *Journal of Applied Meteorology*, 41(12), 1277–1282.
- Cohn, S., Goodrich, R., Morse, C., Karplus, E., Mueller, S., Cornman, L., & Weekley, R. (2001b). Radial velocity and wind measurement with NIMA-NWCA: Comparisons with human estimation and aircraft measurements. *Journal of Applied Meteorology*, 40(4), 704–719.
- Cornman, L., Goodrich, R., Morse, C., & Ecklund, W. (1998). A Fuzzy Logic Method for Improved Moment Estimation from Doppler Spectra. *Journal of Atmospheric and Oceanic Technology*, 15(6), 1287–1305.
- Degreane. (2018a). Acquisition Computer (PCA) - User Manual PCL1300, version T398050S. Written by Marmain, J.
- Degreane. (2018b). Processing Computer (PCT) - User Manual PCL1300, version T398050S. Written by Marmain, J.
- Degreane. (2019). Technical offer - Wind Profiler PCL1300. Written by Sultan, Y.
- Doviak, R. & Zrnić, D. (2006). *Doppler radar and weather observations*. Courier Corporation.
- Fukao, S., Hamazu, K., & Doviak, R. (2014). *Radar for meteorological and atmospheric observations*. Springer.
- Gabor, D. (1946). Theory of communication. Part 1: The analysis of information. *Journal of the Institution of Electrical Engineers-Part III: Radio and Communication Engineering*, 93(26), 429–441.

- Haefele, A. & Ruffieux, D. (2015). Validation of the 1290 MHz wind profiler at Payerne, Switzerland, using radiosonde GPS wind measurements. *Meteorological Applications*, 22, 873–878.
- Hildebrand, P. & Sekhon, R. (1974). Objective determination of the noise level in Doppler spectra. *Journal of Applied Meteorology*, 13(7), 808–811.
- Jordan, J., Lataitis, R., & Carter, D. (1997). Removing ground and intermittent clutter contamination from wind profiler signals using wavelet transforms. *Journal of Atmospheric and Oceanic Technology*, 14(6), 1280–1297.
- Kretzschmar, R., Karayiannis, N., & Richner, H. (2003). Removal of bird-contaminated wind profiler data based on neural networks. *Pattern recognition*, 36(11), 2699–2712.
- Lehmann, V. (2012). Optimal Gabor-frame-expansion-based intermittent-clutter-filtering method for radar wind profiler. *Journal of Atmospheric and Oceanic Technology*, 29(2), 141–158.
- Lehmann, V. & Teschke, G. (2008). Advanced intermittent clutter filtering for radar wind profiler: Signal separation through a Gabor frame expansion and its statistics. *Annales geophysicae* (Vol. 26, 4, pp. 759–783). Copernicus GmbH.
- LTFAT - Søndergaard, P., Balazs, P., Dörfler, M., Holighaus, N., Jaillet, F., Perraudin, N., Průša, Z., Siedenburg, K., Torrésani, B., Wiesmeyr, C., van Velthoven, J., & Necciari, T. (2020). LFAT Reference manual. Retrieved July 17, 2020, from <https://ltfat.github.io/doc/ltfat.pdf>
- MATLAB & Simulink - Calling MATLAB from Python. (2020). Retrieved August 10, 2020, from <https://www.mathworks.com/help/matlab/matlab-engine-for-python.html>
- Mayor, S., Lenschow, D., Schwiesow, R., Mann, J., Frush, C., & Simon, M. (1997). Validation of NCAR 10.6 $\mu$ m CO<sub>2</sub> Doppler lidar radial velocity measurements and comparison with a 915MHz profiler. *Journal of Atmospheric and Oceanic Technology*, 14(5), 1110–1126.
- Merritt, D. (1995). A statistical averaging method for wind profiler doppler spectra. *Journal of Atmospheric and Oceanic Technology*, 12(5), 985–995.
- Meteorology for nuclear accidents - MeteoSwiss. (2020). Retrieved March 17, 2020, from <https://www.meteoswiss.admin.ch/home/measurement-and-forecasting-systems/warning-and-forecasting-systems/meteorology-for-nuclear-accidents.html>

- Radenz, M., Bühl, J., Lehmann, V., Görsdorf, U., & Leinweber, R. (2018). Combining cloud radar and radar wind profiler for a value added estimate of vertical air motion and particle terminal velocity within clouds. *Atmospheric Measurement Techniques*, 11(10).
- Scintec. (2016). Radar Wind Profiler - Theory Manual - LAP Series including RASS. Version 1.02.
- TensorFlow Core - Better performance with the tf.data API. (2020). Retrieved August 10, 2020, from [https://www.tensorflow.org/guide/data\\_performance](https://www.tensorflow.org/guide/data_performance)
- TensorFlow Core - TFRecord and tf.Example. (2020). Retrieved August 10, 2020, from [https://www.tensorflow.org/tutorials/load\\_data/tfrecord](https://www.tensorflow.org/tutorials/load_data/tfrecord)
- Weber, B., Wuertz, D., Strauch, R., Merritt, D., Moran, K., Law, D., Van de Kamp, D., Chadwick, R., Ackley, M., Barth, M. et al. (1990). Preliminary evaluation of the first NOAA demonstration network wind profiler. *Journal of atmospheric and oceanic technology*, 7(6), 909–918.
- Weber, H. (2005). *Classification of contaminated data from wind profiler measurements by neural networks* (Doctoral dissertation, ETH Zurich).
- Weisshaupt, N., Arizaga, J., & Maruri, M. (2018). The role of radar wind profilers in ornithology. *Ibis*, 160(3), 516–527.
- Wilczak, J., Strauch, R., Ralph, F., Weber, B., Merritt, D., Jordan, J., Wolfe, D., Lewis, L., Wuertz, D., Gaynor, J. et al. (1995). Contamination of wind profiler data by migrating birds: Characteristics of corrupted data and potential solutions. *Journal of Atmospheric and Oceanic Technology*, 12(3), 449–467.
- Windprofiler - MeteoSwiss. (2020). Retrieved March 17, 2020, from <https://www.meteoswiss.admin.ch/home/measurement-and-forecasting-systems/atmosphere/windprofiler.html>
- World Meteorological Organization. (2018). *Chapter 5 - special profiling techniques for the boundary layer and the troposphere*. Retrieved May 28, 2020, from [https://library.wmo.int/doc\\_num.php?explnum\\_id=3183](https://library.wmo.int/doc_num.php?explnum_id=3183)